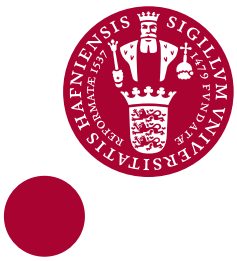

Identification and Description of a Silicic Volcaniclastic Layer in Gale Crater, Mars, Using Active Neutron Interrogation

Czarnecki, S.; Hardgrove, C.; Gasda, Patrick J.; Gabriel, T. S.J.; Starr, M.; Rice, M. S.; Frydenvang, J.; Wiens, R. C.; Rapin, W.; Nikiforov, S.; Lisov, D.; Litvak, M.; Calef, F.; Gengl, H.; Newsom, Horton E.; Thompson, L.; Nowicki, S.

Published in:
Journal of Geophysical Research: Planets

DOI:
10.1029/2019JE006180

Publication date:
2020

Document version
Publisher's PDF, also known as Version of record

JGR Planets

RESEARCH ARTICLE
10.1029/2019JE006180

Key Points:
- A >1 m thick SiO_2- and tridymite-rich layer in Gale crater likely extends over several kilometers
- This layer is stratigraphically conformable, with low water content consistent with significant volcanic glass
- This material is consistent with an evolved igneous material deposited in a lacustrine environment

Supporting Information:
- Supporting Information S1

Correspondence to:
S. Czarnecki,
sean.czarnecki@asu.edu

Citation:
Czarnecki, S., Hardgrove, C., Gasda, P. J., Gabriel, T. S. J., Starr, M., Rice, M. S., et al. (2020). Identification and description of a silicic volcaniclastic layer in Gale crater, Mars, using active neutron interrogation. *Journal of Geophysical Research: Planets*, *125*, e2019JE006180. https://doi.org/10.1029/2019JE006180

Received 22 AUG 2019
Accepted 12 JAN 2020
Accepted article online 30 JAN 2020

Identification and Description of a Silicic Volcaniclastic Layer in Gale Crater, Mars, Using Active Neutron Interrogation

S. Czarnecki[1,2], C. Hardgrove[1], P. J. Gasda[2], T. S. J. Gabriel[1], M. Starr[3], M. S. Rice[3], J. Frydenvang[4], R. C. Wiens[2], W. Rapin[5], S. Nikiforov[6], D. Lisov[6], M. Litvak[6], F. Calef[5,7], H. Gengl[5,7], H. Newsom[8], L. Thompson[9], and S. Nowicki[10]

[1]School of Earth and Space Exploration, Arizona State University, Tempe, AZ, USA, [2]ISR-2: Space Science Applications, Los Alamos National Laboratory, Los Alamos, NM, USA, [3]Geology Department, Western Washington University, Bellingham, WA, USA, [4]Natural History Museum of Denmark, University of Copenhagen, Copenhagen, Denmark, [5]Division of Geological and Planetary Sciences, California Institute of Technology, Pasadena, CA, USA, [6]Space Research Institute, Russian Academy of Sciences, Moscow, Russia, [7]NASA/Jet Propulsion Laboratory-California Institute of Technology, Pasadena, CA, USA, [8]Institute of Meteoritics and Department of Earth and Planetary Sciences, University of New Mexico, Albuquerque, NM, USA, [9]Planetary and Space Science Center, University of New Brunswick, Fredericton, New Brunswick, Canada, [10]ISR-1: Space Science Applications, Los Alamos National Laboratory, Los Alamos, NM, USA

Abstract The Dynamic Albedo of Neutrons instrument aboard the Mars Science Laboratory rover, Curiosity, has been used to map a stratigraphically conformable layer of high-SiO_2 material in Gale crater. Previous work has shown that this material contains tridymite, a high-temperature/low-pressure felsic mineral, interpreted to have a volcanic source rock. We describe several characteristics including orientation, extent, hydration, and geochemistry, consistent with a volcaniclastic material conformably deposited within a lacustrine mudstone succession. Relationships with widely dispersed alteration features and orbital detections of hydrated SiO_2 suggest that this high-SiO_2 layer extends at least 17 km laterally. Mineralogical abundances previously reported for this high-SiO_2 material indicated that hydrous species were restricted to the amorphous (non-crystalline) fraction, which is dominated by SiO_2. The low mean bulk hydration of this high-SiO_2 layer (1.85 ± 0.13 wt.% water-equivalent hydrogen) is consistent with silicic glass in addition to opal-A and opal-CT. Persistent volcanic glass and tridymite in addition to opal in an ancient sedimentary unit indicates that the conversion to more ordered forms of crystalline SiO_2 has not proceeded to completion and that this material has had only limited exposure to water since it originally erupted, despite having been transported in a fluviolacustrine system. Our results, including the conformable nature, large areal extent, and presence of volcanic glass, indicate that this high-SiO_2 material is derived from the product of evolved magma on Mars. This is the first identification of a silicic volcaniclastic layer on another planet and has important implications for magma evolution mechanisms on single-plate planets.

Plain Language Summary Using the Dynamic Albedo of Neutrons instrument aboard the Mars Science Laboratory rover, Curiosity, we mapped a silica-rich layer throughout a small region in Gale crater known as Marias Pass. Previous work has shown that some rocks in Marias Pass contain minerals formed in explosive volcanic eruptions. We determined several key characteristics including orientation, extent, hydration, and elemental composition, which are consistent with material derived from a volcanic deposit. This layer is likely related to nearby silica-rich material deposited by groundwater along subsurface fractures, and geometric relationships to hydrated silica identified from orbit suggest that this high-silica layer extends over at least 17 km. Mineralogical data from previous work indicates the crystalline fraction is anhydrous. As such, we interpret the low hydration of this material, attributable to the amorphous (non-crystalline) fraction, as being consistent with a significant abundance of volcanic glass in addition to other hydrated phases. The presence of volcanic glass indicates that this material has had limited exposure to water since its formation, because glasses tend to preferentially weather. Our results show that this layer is parallel to surrounding rocks, covers a large area, and contains volcanic glass, indicating that it derived from an explosive volcanic product.

1. Introduction

Orbital and surface investigations as well as laboratory analyses of Martian meteorites have shown that the surface of Mars is dominated by basalt (e.g., Agee et al., 2013; McSween, 1984; McSween et al., 2006; McSween, 2015; Mustard et al., 2005; Singer et al., 1979; Taylor et al., 2010), though felsic (e.g., Carter & Poulet, 2013; Christensen et al., 2005; Cousin et al., 2017; Gross & Filiberto, 2014; Humayun et al., 2013; Mangold et al., 2016) compositions have also been identified. Orbital identification of silicic igneous lithologies in various regions of the Martian southern highlands (e.g., Christensen et al., 2005; Wray et al., 2013) lend support to the existence of evolved igneous lithologies on early Mars. Felsic-intermediate compositions are common on Earth where plate tectonics provides a familiar mechanism for magma evolution, but there is a lack of evidence for plate tectonics on Mars, requiring other felsic-intermediate rock formation mechanisms (Bandfield et al., 2000; Wyatt & McSween, 2002).

Recent results from the Mars Science Laboratory (MSL) Curiosity rover have shown evidence for a large diversity of igneous materials in Gale crater, including SiO_2-rich rocks. One such SiO_2-rich deposit is at a location known as "Marias Pass" where Curiosity detected SiO_2 abundances >80 wt.% (Frydenvang et al., 2017) as well as tridymite, a high-temperature/low-pressure SiO_2 polymorph formed in silicic volcanic eruptions (Morris et al., 2016). Hardgrove et al. (2011) demonstrated that high-SiO_2 material in the near subsurface (<50 cm), if it is associated with depleted levels of iron, would have a significant effect on the neutron flux measured by the MSL Dynamic Albedo of Neutrons (DAN) instrument. We use *in situ* neutron spectroscopy provided by the DAN instrument in conjunction with *in situ* geochemical, *in situ* multispectral, and mineralogical results to characterize the extent and hydration of this material in Marias Pass. We also incorporate other surface and orbital observations to map the layer's extent outside Marias Pass and to investigate the implications for its origin.

1.1. Geologic Setting

Since landing in August 2012, Curiosity has been exploring Gale crater, an ~150 km diameter sedimentary basin on Mars. Curiosity has conducted detailed geologic investigations while traversing the crater floor and up the slopes of the ~5 km tall central peak, Aeolis Mons (informally Mount Sharp; Figure 1a). The data returned are used to interpret the depositional environments of geologic units, which include lacustrine, fluvial, and aeolian deposits of primarily basaltic material (Grotzinger et al., 2015). Some of these depositional environments have been interpreted as habitable (Grotzinger et al., 2014) with sedimentary sequences deposited ~3.8–3.6 Ga (Thomson et al., 2011), and possibly as late as ~3.46 Ga with fluvial resurfacing up to ~1.10 Ga (Le Deit et al., 2013).

While traversing up the slopes of Mount Sharp, Curiosity has encountered several rock units including those of the Bradbury group, the Murray formation of the Mount Sharp group, and the Stimson formation of the Siccar Point group (Figure 2). The Murray, which this study focuses on, has a regional dip of ~3° to the northwest (Lewis & Turner, 2019; Kite et al., 2013), away from Mount Sharp. The Murray formation is primarily a lacustrine mudstone (Fedo et al., 2017), though it also contains sandstones and conglomerates (Grotzinger et al., 2015). As of January 2020, over 350 m of Murray stratigraphy has been observed. The lowest exposed unit of the Murray formation is the Pahrump Hills member, a laminated lacustrine mudstone with layers and lenses of cross-stratified fluvial sandstone (Grotzinger et al., 2015; Stack et al., 2019). As shown in Figure 2, the Pahrump Hills member is stratigraphically overlain by the Hartmann's Valley member of the Murray formation and unconformably overlain by the Stimson formation, an aeolian sandstone (Banham et al., 2018; Fraeman et al., 2016).

1.2. Marias Pass

"Pahrump Hills" is the location (Figure 1b) where the geologic member of the same name was first described in detail (Grotzinger et al., 2015), and where the "Telegraph Peak" mudstone drill sample was obtained. Marias Pass, a 20–30 m wide shallow topographic depression, is ~500 m to the southwest (Figure 1b), and 6 m above (Figure 2) Pahrump Hills. Curiosity entered Marias Pass on sol (Martian day) 991 after landing. Marias Pass is located at the approximate midpoint of the Pahrump Hills member stratigraphy (~ −4448 to −4445 m; Figure 2).

Calcium sulfate veins are present throughout the lower Pahrump Hills member (Nachon et al., 2017) as well as in Marias Pass and indicate a postdepositional history of aqueous alteration. Intact calcium sulfate veins present in the Stimson at Marias Pass indicate that alteration continued after the deposition of the Stimson.

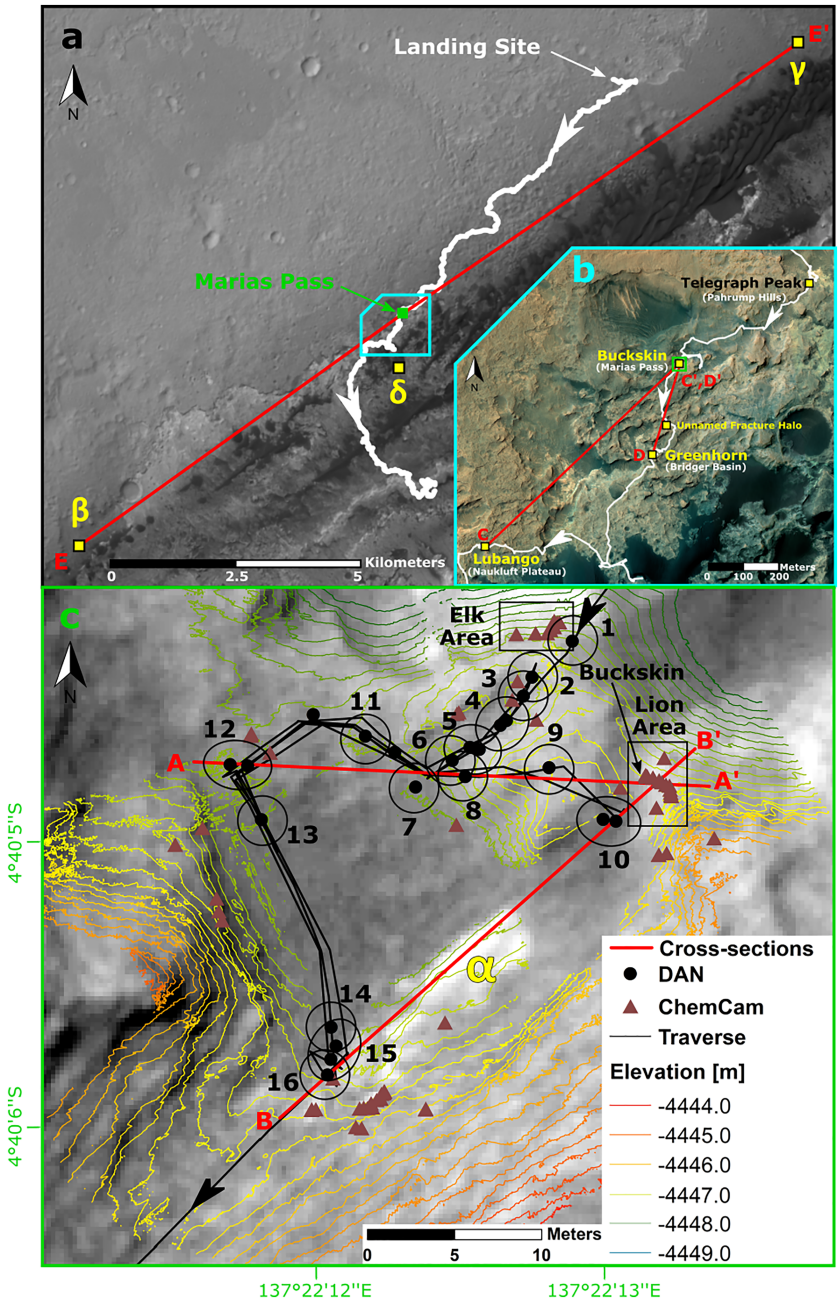

Figure 1. Maps on Mars Reconnaissance Orbiter High-Resolution Imaging Science Experiment image mosaics from Calef and Parker (2016). (a) Map of the Curiosity traverse showing the location of cross section E-E′ (Figure 8e) and orbital (CRISM) detections of hydrated SiO_2 (β, γ, δ). (b) Map of a section of the traverse showing drill locations, an unnamed fracture alteration halo, and cross sections C-C′ and D-D′ (Figures 8c and 8d). Location shown in (a). (c) Map of Marias Pass showing DAN and ChemCam measurements. Location shown in (b). DAN surface footprints for analyzed sites are shown as numbered black ellipses. The location of the Site α Mastcam multispectral image discussed in the text is marked by a yellow α. Cross sections A-A′ and B-B′ are shown in Figures 8a and 8b.

Crosscutting relationships between calcium sulfate veins and high-SiO_2 fracture alteration halos, which we discuss further in section 1.3, indicate that the calcium sulfate veins continued to form during and possibly after alteration halo formation (Frydenvang et al., 2017; Yen et al., 2017).

The goal of our work is to map and characterize high-SiO_2/low-FeO_T material observed in Marias Pass to determine the origin of this anomalous material. The lower ~100 m of Murray stratigraphy (including the Pahrump Hills member) has a mean SiO_2 abundance of 54.4 ± 7.0 wt.% (1σ) and FeO_T abundance of 17.8

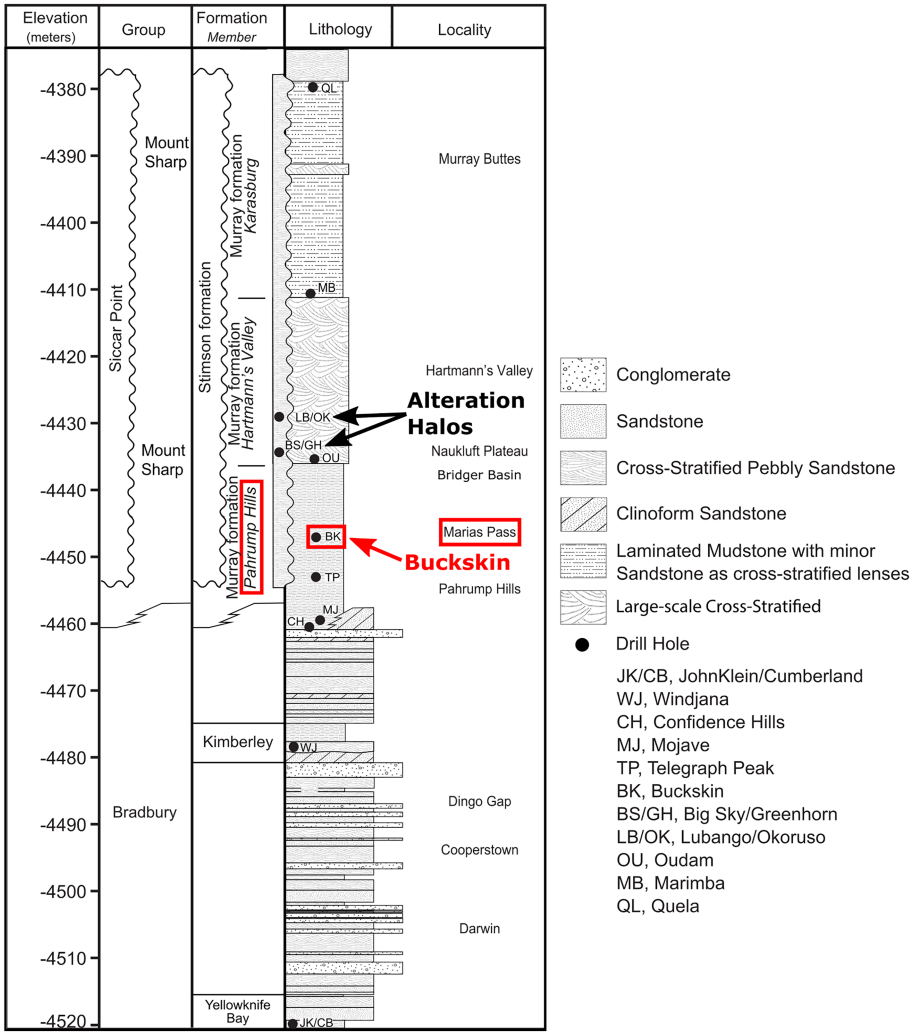

Figure 2. Stratigraphic column showing geologic units defined by the MSL team for the lowest ~145 m of stratigraphy investigated by Curiosity. The Buckskin drill target in Marias Pass is located at about the midpoint of the ~23 m thick Pahrump Hills member, which is primarily composed of laminated lacustrine mudstone.

± 5.2 wt.% (1σ) as measured by the MSL Chemistry and Camera (ChemCam) instrument (Bedford et al., 2019). As reported previously by Frydenvang et al. (2017), SiO_2 abundances ranging from 57–82 wt.% and FeO_T abundances ranging from 2–18 wt.% were observed in the Murray mudstone at Marias Pass. SiO_2 and FeO_T are anticorrelated throughout the Murray (Bedford et al., 2019), including in Marias Pass (Figure 3), where the highest-SiO_2/lowest-FeO_T material was measured in the Murray "Elk" and "Lion" areas exposed on the northern slope of Marias Pass (Figure 1c).

Elevated thermal neutron counts in DAN data were observed at several locations in Marias Pass. This suggested that the subsurface is enriched in hydrogen, depleted in neutron absorbing elements (e.g., iron), or both (these effects are discussed in section 2.1). A drill sample was obtained from the high-SiO_2 target "Buckskin" on sol 1060 (Figures 1 and 3, and Table 1). X-ray diffraction (XRD) experiments with the MSL Chemistry and Mineralogy (CheMin) instrument have shown that Buckskin contains 17.1 ± 1.0 wt.% tridymite and 3.0 ± 0.4 wt.% cristobalite, high-temperature/low-pressure SiO_2 polymorphs commonly formed in felsic-intermediate volcanic eruptions (e.g., Morris et al., 2016; Rampe et al., 2017).

The absence of high-SiO_2 mudstone just above the Lion area suggests that this material is confined to a stratigraphic layer, as suggested by Frydenvang et al. (2017). The DAN instrument is sensitive to differences in the depth distribution of hydrogen and neutron absorbers such as iron in the top ~50 cm of the subsurface,

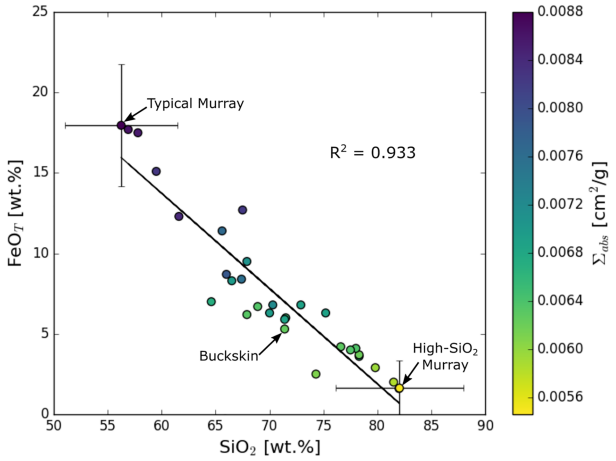

Figure 3. Plot of SiO_2 versus FeO_T for ChemCam targets of Murray mudstone within Marias Pass. Labeled data points are reference geochemistries used in simulations (Table 1). Colors represent macroscopic neutron absorption cross section (Σ_{abs}) for each target. This strong SiO_2-FeO_T anticorrelation demonstrates that low-Σ_{abs} (low-FeO_T) compositions in Marias Pass can be interpreted as having high-SiO_2 abundances. These data were first reported by Frydenvang et al. (2017). Representative error bars are provided for end-member compositions.

allowing us to determine the depth distribution of the high-SiO_2/low-FeO_T material in Marias Pass and map its extent and relationship to other SiO_2-rich deposits in the Murray and Stimson formations.

1.3. Fracture Alteration Halos

A rare exposure of the Murray/Stimson unconformity is at the southern end of Marias Pass (Banham et al., 2018). Several light-toned alteration zones surrounding fractures have been discovered in Gale crater, including in the Stimson just above the exposed unconformity in Marias Pass (Figure 4). Upsection from Marias Pass, drill samples were taken from fracture alteration halo targets and nearby unaltered bedrock targets in the Stimson. The alteration halo target "Greenhorn" is located in "Bridger Basin" ~300 m south of and ~10 m above Marias Pass, and the alteration halo target "Lubango" is located in "Naukluft Plateau" ~640 m southwest of and ~5 m above Bridger Basin (Figure 1b). Geochemical analyses of sample drill tailings show that these alteration halos have elevated SiO_2 content (53–60 wt.%) relative to nearby unaltered bedrock targets (43–45 wt.%) (Yen et al., 2017). Unlike Buckskin, these high-SiO_2 alteration halo samples did not contain tridymite. The association of these alteration halos with fractures indicates their formation is a result of aqueous alteration that post-dated the lithification of the Stimson formation (Frydenvang et al., 2017; Yen et al., 2017). Other light-toned fracture alteration halos have been observed elsewhere in the Stimson formation (Banham et al., 2018), in the Murray formation (Frydenvang et al., 2017; Gasda et al., 2016; Yen et al., 2017), and in the Bradbury group.

The SiO_2 enrichment mechanism which formed these alteration halos has been debated in the literature and hypotheses include both passive enrichment through acid leaching and active enrichment through SiO_2 sintering. Yen et al. (2017) argued that the Stimson alteration halos were passively enriched in SiO_2 through an acid leaching process in which acidic fluids preferentially remove some geochemical species, leaving relatively more SiO_2 behind. This is consistent with some geochemical differences observed between the altered and unaltered Stimson samples. Evolved Gas Analysis (EGA) by the MSL Sample Analysis at Mars (SAM) instrument of the Greenhorn sample has shown reduced nitrate and oxychlorine abundances relative to nearby unaltered Stimson material (Sutter et al., 2017). This is also consistent with an acid leaching event during the formation of the Stimson alteration halos. Alternatively, it has been suggested that the Stimson high-SiO_2 alteration halos were actively enriched in SiO_2 via mobilization from an underlying source in the Murray formation (Frydenvang et al., 2017; Yen et al., 2017). This helps explain the large SiO_2 enrichment observed in the Stimson halos, which is unlikely to be entirely due to acid leaching, and it is possible that both passive and active enrichment occurred in multiple diagenetic (postdepositional alteration) stages (Yen et al., 2017). Additionally, CO_2 releases detected by the SAM instrument from the Greenhorn drill sample are consistent with the presence of minor carbonates, which in turn would indicate that alkaline alteration occurred after acidic alteration in this halo (Sutter et al., 2017). The most likely source for the SiO_2 mobilized into the Stimson alteration halos is the tridymite-bearing material observed in Marias Pass that underlies the Stimson (Frydenvang et al., 2017).

2. Methods

We determined the layered geochemical structure and hydration of 16 sites covering the area of Curiosity's traverse in Marias Pass and identified another location consistent with a high-SiO_2/low-FeO_T composition. This involved integrating compositional data from the DAN, ChemCam, Alpha Particle X-ray Spectrometer (APXS), and Mast Camera (Mastcam) instruments aboard the Curiosity rover.

2.1. Instruments

DAN is a neutron spectrometer with passive and active modes, which is composed of a pulsed neutron generator (PNG) and two He-3 neutron detectors. In passive mode, DAN detects neutrons created by galactic cosmic ray spallation in the Martian subsurface. These data are gathered while the rover is stationary as well as during rover mobility (Jun et al., 2013). In active mode, the PNG produces 14.1 MeV neutrons over

Table 1
Bulk Mineralogy, SiO_2, FeO_T, and Cl Abundances of Modeled Geochemistries

	Baseline Marias Pass Murray Bedrock[a]	High-SiO_2 Murray Bedrock[b]	Buckskin[c]	Telegraph Peak[d]
SiO_2[e]	56.3 ± 5.2	82.0 ± 5.9	71.0 ± 5.4	51.4 ± 5.0
FeO_T[e]	18.0 ± 3.8	1.63 ± 1.70	5.60 ± 2.10	18.7 ± 3.9
Cl[f]	0.34 ± 0.01	0.34 ± 0.01	0.34 ± 0.01	0.34 ± 0.01
Σ_{abs}[g]	0.0088 ± 0.0011	0.0055 ± 0.0007	0.0065 ± 0.0007	0.0086 ± 0.0009
Plagioclase	—	—	17.1 ± 1.2	27.1 ± 2.8
Sanidine	—	—	3.4 ± 0.7	5.2 ± 2.2
Magnetite	—	—	2.8 ± 0.3	8.2 ± 0.9
Hematite	—	—	—	1.1 ± 0.5
Quartz	—	—	—	0.9 ± 0.4
Anhydrite	—	—	0.7 ± 0.2	—
Tridymite	—	—	13.6 ± 0.8	—
Cristobalite	—	—	2.4 ± 0.3	7.3 ± 1.7
Other[h]	—	—	—	12.1 ± 3.6
Opal-CT	—	—	6.0	10.9
Amorphous	—	—	54	27.2 ± 15

Note. Oxide, elemental, and mineral abundances are listed in wt.%.
[a]SiO_2 and FeO_T averaged from "Mission," "Piegan," and "Fisch_Scale," representative low-SiO_2 endmember ChemCam targets in Marias Pass and Bridger Basin. Cl abundance from APXS of Telegraph Peak drill tailings. No drill sample taken for mineralogical analysis. [b]SiO_2 and FeO_T averaged from high-SiO_2 endmember ChemCam targets in the "Lion," "Elk," and "Meeteetse" areas in Marias Pass and Bridger Basin. Cl abundance from APXS of Buckskin drill tailings. No drill sample taken for mineralogical analysis. [c]SiO_2 and FeO_T from "Blind_Gulch" ChemCam target at the Buckskin drill hole. Cl abundance from APXS of Buckskin drill tailings. Mineralogy from Morris et al. (2016). [d]SiO_2 and FeO_T from "Telegraph_Peak_ccam" ChemCam target. Cl abundance from APXS of Telegraph Peak drill tailings. Mineralogy from Rampe et al. (2017). [e]SiO_2 and FeO_T reported with accuracy uncertainties from ChemCam. [f]Cl reported with precision uncertainties from APXS. [g]Macroscopic thermal neutron absorption cross section (Σ_{abs}) is a measure of the probability that a material will absorb thermal neutrons, reported in cm^2/g. [h]Other crystalline components include forsterite, pigeonite, orthopyroxene, and fluorapatite. See Rampe et al. (2017) for abundances.

a typical measurement duration of 20 min. The time-of-flight and energy of neutrons, which return to the detectors, are dependent on the subsurface composition, primarily hydrogen (which efficiently scatters neutrons, reducing kinetic energy) and elements like iron and chlorine which increase the macroscopic thermal neutron absorption cross section (Σ_{abs}), a measure of the probability that a material will absorb thermal neutrons. DAN detects neutrons scattered within the top ~50 cm. Since both hydrogen and iron are very efficient at thermalizing and absorbing neutrons, respectively, DAN is sensitive to abundances of these species in the Martian subsurface (e.g., Hardgrove et al., 2011; Mitrofanov et al., 2012; Sears, 1992) as well as their depth distribution (e.g., Gabriel et al., 2018). Further details on the DAN instrument and its operation can be found in the literature (Litvak et al., 2008; Mitrofanov et al., 2012).

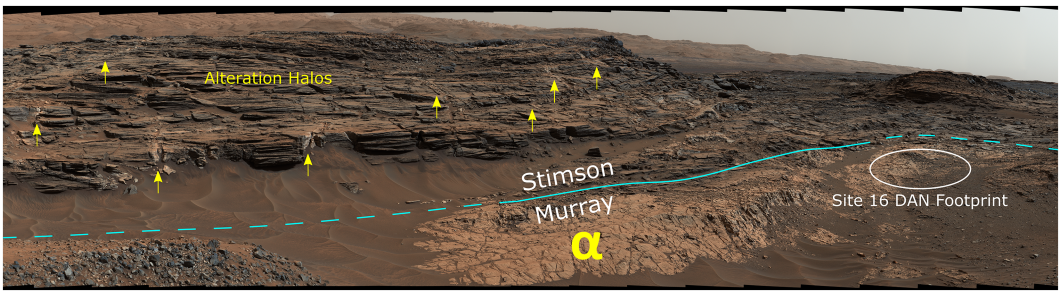

Figure 4. Portion of Mastcam mosaic mcam04395 looking south, showing the southeastern area of Marias Pass including Sites 16 and α. Light-toned fracture alteration halos are visible in the overlying Stimson sandstone. Similar light-toned Stimson alteration halos were analyzed upsection at "Greenhorn" and "Lubango" and are enriched in SiO_2. Mastcam image IDs are listed in section S1 in the supporting information.

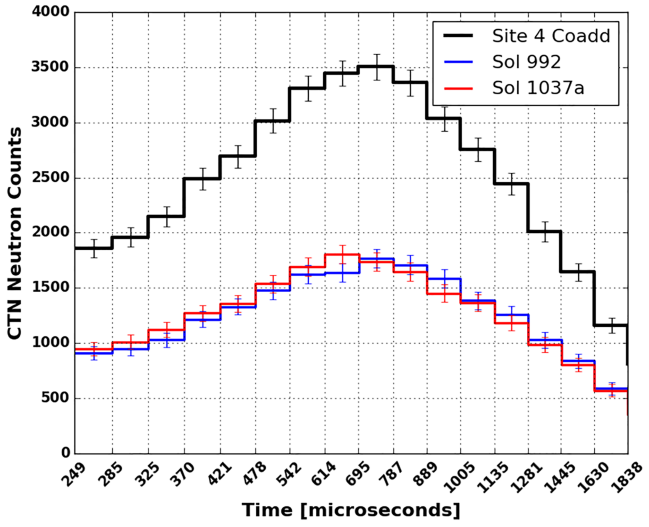

Figure 5. Example of coadded DAN active measurements. Shown are DAN CTN (thermal neutron) data for sols 992 and 1037a, which were coadded for Site 4, plotted along with the coadded data. Measurements are only coadded if they are spatially proximal and exhibit similar die-away curves. Because measurement uncertainty is statistical, the coadded measurement has better precision than either constituent measurement.

To derive results from DAN, we compare DAN data to simulation data, which incorporates *in situ* geochemical abundances from the ChemCam and APXS instruments. ChemCam uses Laser-Induced Breakdown Spectroscopy (LIBS), which ablates material from a target up to 7 m away and records the spectrum of the resulting plasma over the 240–905 nm wavelength range (Clegg et al., 2017; Maurice et al., 2012; Wiens et al., 2012). Typically, a raster of several LIBS target points (e.g., 5 × 1 or 3 × 3) is performed and 30 LIBS shots are taken per point, with each point being 300–500 μm in diameter. The first five shots are removed from analyses due to surficial target dust contamination. The APXS sensor head is located on the rover arm and can be placed in contact with selected targets. Curiosity is equipped with a dust removal tool to minimize the effect of dust cover for APXS surface measurements. Further details on the APXS instrument can be found in the literature (e.g., Campbell et al., 2014). Several elements, such as silicon and iron are quantified by both ChemCam and APXS. Since the geochemistry varies considerably in Marias Pass, we primarily use ChemCam-derived geochemistries because the small ChemCam spotsize and larger data set captures more geochemical variability. But because ChemCam does not typically quantify chlorine abundance, we use chlorine abundances determined by APXS from nearby and geochemically similar targets in our analyses.

The Mastcam instrument is a pair of charge-coupled device cameras with fixed focal lengths (34 mm in the left camera and 100 mm in the right camera) mounted roughly 2 m above the surface on the rover's mast (Malin et al., 2017). Each camera obtains images through a Bayer pattern of red, green, and blue filters and telecentric microlenses bonded onto the charge-coupled device and an eight-position narrowband filter wheel that provides the ability to obtain spectra in 12 unique wavelengths between 445 and 1013 nm (Bell III et al., 2017).

2.2. DAN Active Data Analysis

After each pulse from the DAN PNG, neutrons from each detector are counted and recorded in 64 lognormal time bins totaling 0.1 s. Total counts for each bin are summed over all pulses for a given measurement, resulting in what is known as a neutron "die-away" curve because the neutron signal first increases then decreases back to the background level. We subtract the background galactic cosmic ray-induced neutron count rate, weighted by bin width, from each time bin as in Gabriel et al. (2018). See Gabriel et al. (2018) for further DAN active preprocessing details.

To improve the statistical precision of data from those DAN active measurements with a signal-to-noise ratio (SNR) less than 5, we coadded (summed the neutron counts on a bin-by-bin basis) multiple such measurements together as performed in Gabriel et al. (2018). Measurements are only coadded if they are proximal both laterally (within 2–3 m) and topographically (within 2–3 cm vertically), and there is no significant visible change in the material exposed at the surface, determined using rover camera imagery (Abercrombie et al., 2019). Die-away curves for each coadded measurement are also compared to ensure thermal neutron peak location, relative peak height, etc., are similar. DAN active measurements that had an SNR less than 5 for any time bin used in our analysis and could not be coadded to improve SNR, were not included in our final results. Figure 5 is an example showing the individual die-away curves of the two DAN active measurements coadded for Site 4, as well as the coadded die-away curve. Section S2 of the supporting information describes the process of DAN active collocation and coaddition used in this work.

To estimate the subsurface geochemical composition, we use a forward modeling scheme where the thermal neutron die-away data measured with DAN is compared to synthetic die-away data produced in simulations using the Monte Carlo N-Particle 6 (MCNP6) particle transport code (Werner et al., 2018). These simulations model a 3-dimensional environment, which includes the DAN PNG and detectors, a rover model, the Martian atmosphere, and various subsurface geochemistries. We achieved a relative statistical uncertainty <5% for neutron counts in each analyzed time bin in every simulation used for this study. We use the same MCNP6 input file as that used by Gabriel et al. (2018) with subsurface geochemical abundances from ChemCam and chlorine from APXS. Table 1 lists the SiO_2, FeO_T, Cl, Σ_{abs}, and mineralogy for the two

Table 2
Parameter Ranges for Model Grids Used in MCMC Analyses

Model grid	WEH range (wt.%)	Σ_{abs} Range (cm^2/g)	Depth range (cm)
1	0.2–6.0	0.0042–0.0237	-
2A	Top: 1.4–3.8	Top: 0.0088	5–25
	Bottom: 0.2–3.0	Bottom: 0.0055–0.0086	
2B	Top: 1.8–3.4	Top: 0.0063–0.0101	5–25
	Bottom: 1.2–2.8	Bottom: 0.0055	

in situ geochemistries used in our models ("Baseline Marias Pass Murray Bedrock" and "High-SiO_2 Murray Bedrock") along with the Buckskin and Telegraph Peak geochemistries for reference. The SiO_2, FeO_T, and Σ_{abs} are derived from ChemCam data of specific targets (listed in the table notes) and Cl values are from relevant APXS targets (listed in the table notes). The APXS target "Wallace" is the nearest APXS measurement to the Marias Pass ChemCam targets used to generate the Baseline Marias Pass Murray Bedrock geochemistry. The Wallace Σ_{abs} of 0.0092 ± 0.0001 cm^2/g agrees with the Baseline Marias Pass Murray Bedrock value of 0.0088 ± 0.0011 cm^2/g. No APXS measurements were taken at the locations of the Marias Pass ChemCam measurements used to create the High-SiO_2 Murray Bedrock geochemistry. The APXS Buckskin drill tailings Σ_{abs} value of 0.0060 ± 0.0001 cm^2/g agrees with the ChemCam Buckskin value of 0.0065 ± 0.0007 cm^2/g and the APXS Telegraph Peak drill tailings Σ_{abs} value of 0.0089 ± 0.0001 cm^2/g agrees with the ChemCam Telegraph Peak value of 0.0086 ± 0.0009 cm^2/g. We conducted simulations to test the effect of calcium sulfate veins on derived DAN results since these veins are present throughout the Murray stratigraphy (Vaniman et al., 2018). In section S3 of the supporting information we demonstrate that these veins are not in sufficient volumetric abundance in the subsurface to have a measurable effect on our analysis of data in this region.

Depending on the type of model, we vary several parameters including layer thickness/depth, hydrogen abundance, and Σ_{abs}. The parameters spanned by our "grids" of models are listed in Table 2. Our initial simulations for each site used a one-layer subsurface model grid in which individual models varied both hydrogen abundance (reported as water-equivalent hydrogen or WEH) as well as iron and chlorine (as proxies for Σ_{abs}) in a homogeneous subsurface. In order to span the range of Σ_{abs} observed in Gale crater, our one-layer models vary iron between 0.48 and 14.22 wt.% and chlorine between 0.1 and 3.0 wt.%. Most sites in Marias Pass fit best with lower-Σ_{abs} values than the Σ_{abs} of Baseline Marias Pass Murray Bedrock (Table 1). Sites that had significant sand/rubble cover within the DAN field of view, or with a surface bedrock geochemistry that was inconsistent with the Σ_{abs} of the best fit one-layer models, were analyzed using one or both of the two-layer model grids. All two-layer models used in this study varied hydrogen abundance and depth for each layer. Model Grid 2A varied the bottom layer geochemistry with the top layer set to the Baseline Marias Pass Murray Bedrock geochemistry, and Model Grid 2B varied the top layer geochemistry with the bottom layer set to the High-SiO_2 Murray Bedrock geochemistry (Table 2). Chlorine abundances measured by APXS of drill tailings from the Telegraph Peak and Buckskin samples are both 0.34 ± 0.01 wt.% (Table 1), indicating that chlorine does not vary significantly between the high-SiO_2 Buckskin material and the Murray immediately downsection, which was sampled at Telegraph Peak. No other elements measured by ChemCam and APXS contribute enough to the Σ_{abs} of these samples to be responsible for significant variations in Σ_{abs}. The low Σ_{abs} determined for most DAN active measurements analyzed in this work (see section 3) do not allow for significant abundances of other efficient neutron absorbers, which are not measured by ChemCam or APXS, without requiring Fe or Cl to have nonphysical negative abundances. For the above reasons, we take the variations observed in Σ_{abs} to be the result of variable FeO_T, following the trend seen in Figure 3. Section S4 in the supporting information describes the process of model generation and implementation for the modeling grids used in this work.

To compare DAN data to MCNP6 simulation data, we analyze the time bins with the most dynamic thermal neutron count rates (from 249–1838 μs after the pulse). At ~249 μs, the PNG-induced epithermal neutron count rate falls to background levels, so the background-subtracted neutron count rate is due to only thermal neutrons. The area under the die-away curve in this range is normalized for both the DAN data and the simulation data (Gabriel et al., 2018). Using the data processing and analysis pipeline from Gabriel et al. (2018), a Markov-Chain Monte Carlo (MCMC) analysis is performed to evaluate the active DAN data across

Table 3
Results From MCMC Analyses of Sites 1-16

Site	Sol[a]	WEH (wt.%)[b]	Σ_{abs} (cm^2/g)[b]	Depth (cm)[c]	Model Grid
1	991	1.88 ± 0.29	0.0053 ± 0.0003	—	1
2	1037c	2.08 ± 0.38	0.0080 ± 0.0004	—	1
3	1037b	2.59 ± 0.32	0.0058 ± 0.0003	—	1
4	992, 1037a	2.74 ± 0.32	0.0056 ± 0.0003	—	1
5	1035d, 1042a	2.03 ± 0.37	0.0055[d]	12.0 ± 4.6	2B
6	1035c	1.92 ± 0.41	0.0055[d]	12.1 ± 4.5	2B
7	1035b	2.01 ± 0.32	0.0055 ± 0.0003	—	1
8	1049	1.54 ± 0.52	0.0055[d]	14.3 ± 4.0	2B
9	1051	1.54 ± 0.25	0.0046 ± 0.0003	—	1
10	1053, 1056	1.76 ± 0.41	0.0055[d]	12.4 ± 4.3	2B
11	1042b	2.03 ± 0.46	0.0126 ± 0.0009	—	1
12	1044a, 1066	1.22 ± 0.31	0.0110 ± 0.0007	—	1
13	1044b	0.92 ± 0.23	0.0090 ± 0.0005	—	1
14	995	0.93 ± 0.25	0.0074 ± 0.0005	—	1
15	1030, 1067	0.94 ± 0.37	0.0061 ± 0.0005	10.3 ± 5.1	2A
16	997–1028	1.36 ± 0.38	0.0060 ± 0.0004	10.2 ± 4.7	2A

Note. Both one- and two-layer models were used in Marias Pass, with two-layer models only being used when the surface geochemistry did not agree with one-layer-modeled Σ_{abs} fit values.
[a]A sol number including an a, b, c, or d refers to the first, second, third, or fourth measurement taken on that sol, respectively. Measurements with multiple sols listed have been coadded (see section 2.2). Site 16 is coadded from all six measurements in the listed sol range. [b]Reported WEH and Σ_{abs} are bulk values for one-layer models and high-SiO_2 layer values for multiple-layer models. [c]Burial depth of high-SiO_2 material in the bottom layer of a two-layer model [d]Bottom layer geochemistry for these sites was set to the High-SiO_2 Murray Bedrock geochemistry (Table 1) based on preliminary one-layer model results (see section S4 in the supporting information).

the modeled grid of simulations. See section S5 in the supporting information, Gabriel et al. (2018), and Foreman-Mackey et al. (2013) for further details concerning MCMC analyses.

2.3. Mastcam Multispectral Data Analysis

Mastcam multispectral observations (Table S1 in the supporting information) were acquired at Marias Pass and at nearby fracture alteration halos with elevated SiO_2 and low FeO_T. Spectra from the high-SiO_2/low-FeO_T targets were compared to those from other observations of Murray rocks to determine spectral characteristics that distinguish high-SiO_2/low-FeO_T materials in Mastcam spectra. Spectra from additional Marias Pass targets (at Site α) were then evaluated for these characteristics. See section S6 in the supporting information for further details concerning our Mastcam multispectral analysis.

3. Results

The results of MCMC analyses for each investigated DAN active site are listed in Table 3. WEH is a unit that represents the water abundance if all measured hydrogen is in the form of H_2O, and Σ_{abs} is the macroscopic thermal neutron absorption cross section. Sites 1–10 are located in northeastern Marias Pass, and DAN results show that all but one of these sites have relatively low-Σ_{abs}, which is consistent with a high-SiO_2/low-FeO_T composition (Figure 3). DAN results show that Sites 5, 6, 8, and 10 contain over 10 cm of unconsolidated material covering low-Σ_{abs} bedrock consistent with a high-SiO_2/low-FeO_T composition. Sites 15 and 16, in southern Marias Pass, also are shown to contain relatively low-Σ_{abs} material beneath over 10 cm of Baseline Marias Pass Murray Bedrock (Figure 1). Results from Sites 2 (in northeastern Marias Pass), 11–13 (in northwestern Marias Pass), and 14 (in southern Marias Pass) are not consistent with low-Σ_{abs} material, likely due to unconsolidated bedrock fragments and/or windblown sand in the top ~50 cm. The hydration of subsurface low-Σ_{abs} material in Marias Pass ranges from 0.94–2.74 wt.% WEH.

Plots showing the results of our DAN active MCMC analyses are available in Figures S1–S16 in the supporting information. An example plot is shown in Figure 6 for Site 16. Site 16, on the south side of Marias

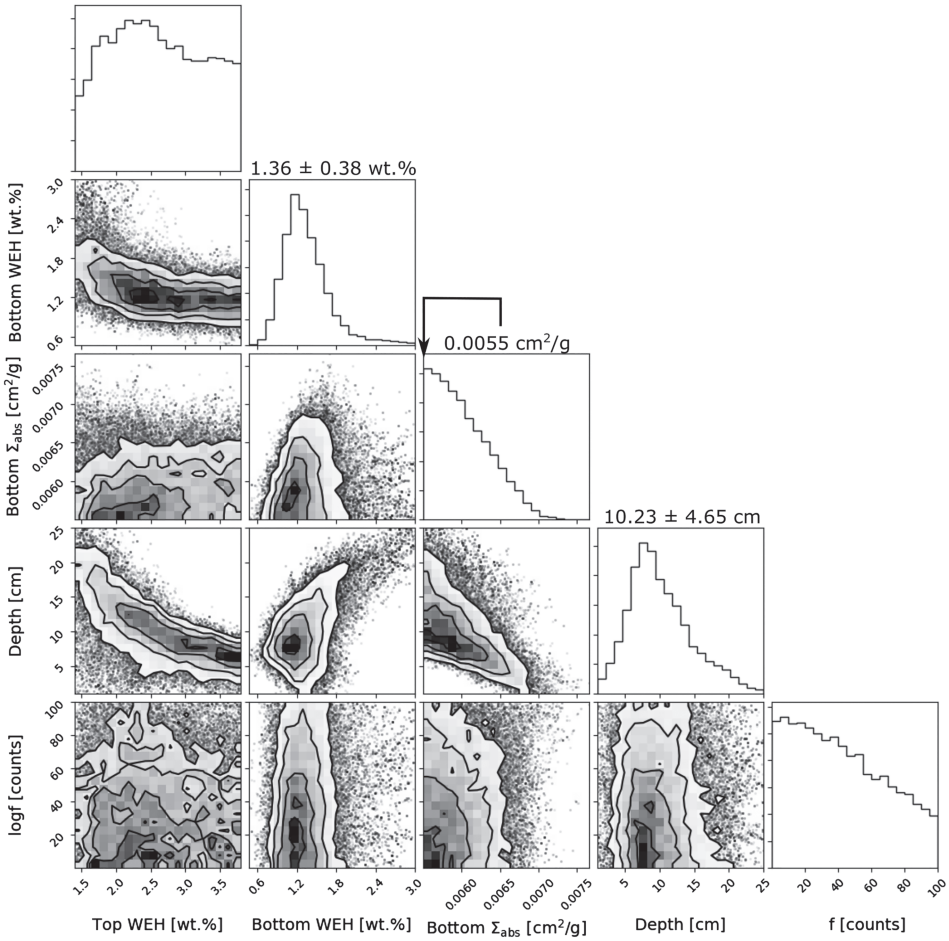

Figure 6. Corner plot showing MCMC free parameter posterior distributions of models at Site 16 (Figures 1c and 4). Nondiagonal frames represent 2-D posterior distributions and are used to understand instrument response to multiple parameters and the measurement degeneracy. The diagonal frames represent the 1-D (marginalized) posterior distribution and are used to determine the optimized value of the free parameters (shown above the frames). This analysis most strongly discriminates the value of the lower layer water content (1.36 ± 0.38 wt.%) and the depth to the bottom layer (10.23 ± 4.65 cm). The top layer water content is not strongly constrained by this analysis, likely due to the fact that it is thin (as shown by the depth result). The lower layer contains a low-Σ_{abs} material consistent with the lowest-Σ_{abs} material observed in Marias Pass (0.0055 barns). The "f" parameter parameterizes underestimated uncertainty. See Figures S1–S16 in the supporting information for corner plots of each site.

Pass, is ~25 m southwest of the high-SiO_2 material exposed at the Lion area (Figures 1c and 4). MCMC analysis shows that a low-Σ_{abs} material is buried beneath surface bedrock. This low-Σ_{abs} material does not match the geochemistry of the bedrock exposed at the surface, but is consistent with the highest-SiO_2/lowest-FeO_T material present in the Lion area.

We also find that trends in DAN passive data in the Marias Pass region are consistent with our DAN active results above. In the vicinity of Sites 1–8 the mean passive neutron count rate is relatively high (61.9 neutrons per second), suggesting elevated hydrogen content and/or lower neutron absorber content. Lower mean passive count rates in the vicinity of Sites 11–13 (29.7 neutrons per second) and moderate mean passive count rates near Sites 14–16 (37.6 neutrons per second) suggest a lower level of hydration and/or higher neutron absorber content near these sites. These DAN passive count rate trends are consistent with a high abundance of high-SiO_2/low-FeO_T material near sites 1–8, a lower abundance of high-SiO_2/low-FeO_T material near sites 14–16, and no high-SiO_2/low-FeO_T material near sites 11–13.

In Mastcam spectra, the high-SiO_2/low-FeO_T targets from the observations listed in Table S1 in the supporting information were found to exhibit small 937 nm band depths and steep blue-to-red (447–638 nm) slopes compared to other rock targets in the Murray formation (Figure 7). The 937 nm band depth is defined

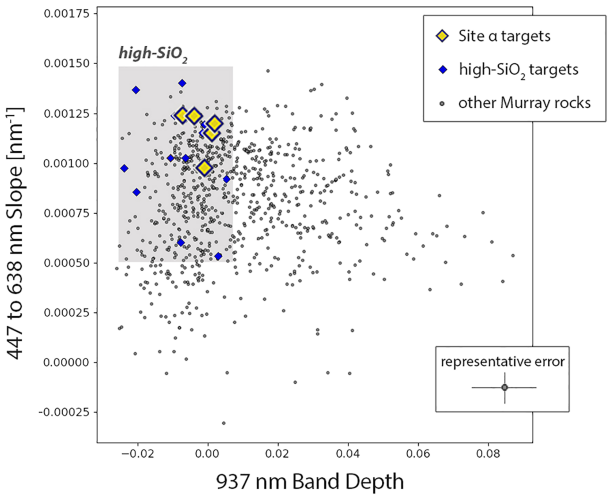

Figure 7. Mastcam parameter-space plot comparing spectra of high-SiO_2/low-FeO_T targets to spectra of other rock targets in the Murray formation. The shaded region indicates a Mastcam-based spectral characterization of the high-SiO_2/low-FeO_T targets at Marias Pass and nearby fracture alteration halos (observations listed in Table S1 in the supporting information): high values of the blue-to-red slope (447–638 nm) and small to negative values of the 937 nm band depth (measured beneath a continuum line with shoulder positions at 805 and 1013 nm). Representative error bars for each parameter are calculated from uncertainties in the relative band-to-band reflectance. Spectra from Site α share the same spectral characteristics of known high-SiO_2/low-FeO_T targets. This is consistent with the prediction, based on DAN active analysis, that Site α exposes high-SiO_2/low-FeO_T bedrock. See Figures 1c and 4 for Site α location.

as the percent drop in R^* at 937 nm beneath a continuum line with shoulder positions at 805 and 1013 nm. This parameter indicates the presence of the broad Fe^{2+} absorption in iron-bearing primary basaltic minerals (e.g., Clark et al., 1990). The absence of this absorption (as indicated by negative band depth values) can be an indicator of iron depletion. The blue-to-red slope is an indicator of the overall "redness" of the visible spectrum and is strongly influenced by nanophase iron oxide in Mars' ubiquitous red surface dust, which exhibits a steep ~400–600 nm iron-oxygen charger transfer absorption edge. Light-toned rocks are more easily "reddened" by a thin layer of surface dust than are dark-toned mafic rocks. Therefore, high blue-to-red slope values can indicate bright but otherwise spectrally bland materials, as would be expected for the spectra of high-SiO_2/low-FeO_T targets (e.g., Smith et al., 2013). SiO_2-rich rocks observed by the Mars Exploration Rover Spirit's Pancam (a multispectral camera system similar to Mastcam) at Gusev crater were also characterized by large blue-to-red spectral slopes (Rice et al., 2010).

Although these spectral characteristics are not unique to the high-SiO_2/low-FeO_T targets, they are consistent among this compositional class and can be used to determine whether other surface targets are spectrally similar. Indeed, Figure 7 shows that Mastcam spectra of rocks at Site α (from the "Red Horn" and "Red Sheep" targets) fall within the same region of this parameter space as all other known high-SiO_2/low-FeO_T targets. The specific bounds on these parameters (gray box in Figure 7) exclude 70% of the other 832 rock spectra from the Murray formation analyzed here.

4. Discussion

4.1. Orientation and Extent of High-SiO_2 Layer

4.1.1. Subsurface Expression in Marias Pass

Sites 1, 3–10, 15, and 16 all contain material in the subsurface that has a Σ_{abs} value consistent with high-SiO_2/low-FeO_T material measured by ChemCam and APXS in the Elk and Lion areas ("Hi-SiO_2 Murray" and "Buckskin" in Figure 3 and Table 1). Mastcam multispectral analysis (Figure 7) of Site α is also consistent with the high-SiO_2/low-FeO_T material exposed in the Elk and Lion areas. Sites 2 and 11–14 do not contain high-SiO_2/low-FeO_T material within the DAN field of view, suggesting that the top ~50 cm of the subsurface is detrital material transported from another location that filled in an eroded volume. This is supported by rover imagery showing a heterogeneous mixture of transported bedrock fragments and sand at the surface in this area (see section S4 in the supporting information).

A single subhorizontal layer can project through all high-SiO_2/low-FeO_T material observed in Marias Pass, and our depth results constrain the thickness and orientation of this layer. Figures 8a and 8b are cross sections within Marias Pass, locations of which are shown in Figure 1c. Relationships shown in Figure 8a require a layer thickness of at least 1 m. The Lion area, Sites 5–10, and Site 12 are approximately colinear (for clarity, Figure 8a only shows results from Site 8 of those near the center of the cross section). Since the upper and lower contacts of the high-SiO_2/low-FeO_T layer are not observed within the DAN field of view at these sites, the east-west dip (stratigraphic layer orientation relative to horizontal) is unknown, but we note that a smaller or larger dip angle than that shown in Figure 8a requires a thicker high-SiO_2/low-FeO_T layer. The dip from the Lion area to the top of the high-SiO_2/low-FeO_T material at Site 16 is at most 0.6° southwest (Figure 8b). The Murray has a regional dip of ~ 3° northwest (Kite et al., 2013; Lewis & Turner, 2019), and the orientation of the high-SiO_2/low-FeO_T layer in Marias Pass is consistent with a minor local variation of this dip.

4.1.2. Relationship to High-SiO_2 Fracture Alteration Halos

Mass balance calculations using the amorphous (noncrystalline) phase fraction, relative crystalline phase abundances, and absolute geochemical abundances of drill samples indicate that the amorphous component of the Buckskin high-SiO_2 bedrock (Morris et al., 2016) and Greenhorn and Lubango high-SiO_2 fracture alteration halos (Yen et al., 2017) contain little or no Al_2O_3. Other oxides including SiO_2, FeO_T, MgO, Na_2O,

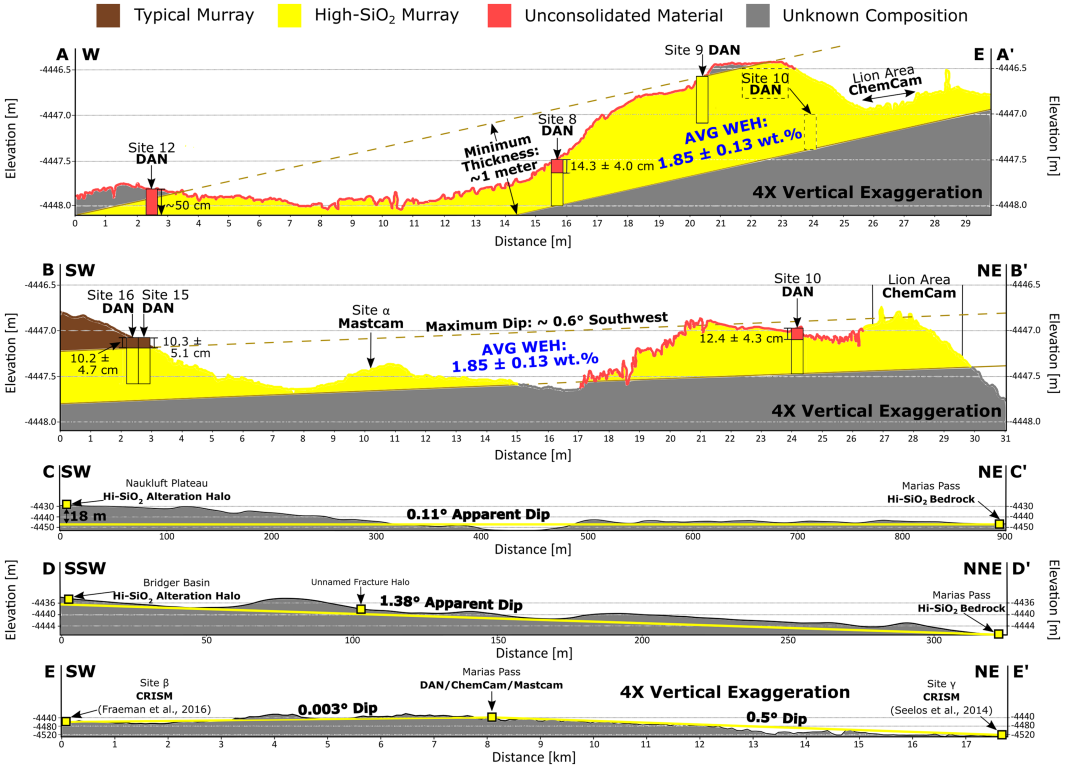

Figure 8. Topographic cross sections (locations shown in Figure 1). A-A′ and B-B′ show interpreted subsurface compositions based on DAN-derived Σ_{abs} values and surface compositions from ChemCam/Mastcam analyses. (a) Cross section from Site 12 to the Lion area, 4X vertical exaggeration. One possible high-SiO_2/low-FeO_T layer dip is shown, but the dip component in this direction is not constrained. The minimum thickness of the high-SiO_2/low-FeO_T layer is constrained by DAN results from Sites 8–10. Site 10 bedrock (dashed, located about 2 m south of A-A′) is projected from its measured elevation. Site 9 is covered by a thin (<5 cm) veneer of sand but was modeled as a single layer to reduce simulation complexity (see section S4 in the supporting information). (b) Cross section from Site 16 to the Lion area, 4X vertical exaggeration. Relationships shown here constrain the maximum dip of the high-SiO_2/low-FeO_T layer in this direction. (c, d) Cross sections from Marias Pass to Naukluft Plateau (location of the Lubango fracture alteration halo) and Bridger Basin (location of the Greenhorn fracture alteration halo). The projected apparent dip of the high-SiO_2/low-FeO_T layer, based on a true regional dip of 3° northwest (Kite et al., 2013; Lewis & Turner, 2019) is 0.11° and 1.38° from Marias Pass to Lubango and Greenhorn, respectively. This places the high-SiO_2/low-FeO_T layer ~18 m below Lubango, ~2 m below Greenhorn, and ~1.5 m below an unnamed alteration halo. These vertical proximities support the hypothesis that the high-SiO_2/low-FeO_T bedrock was a source for the SiO_2 enrichment of the overlying alteration halos. (e) Cross section passing through Marias Pass and hydrated SiO_2 deposits observed by CRISM (Fraeman et al., 2016; Seelos et al., 2014), 4X vertical exaggeration. <0.5° dips are required for stratigraphic equivalence between Marias Pass and Sites β and γ, consistent with a 3° regional dip to the northwest.

and P_2O_5 all have similar abundances in the high-SiO_2 bedrock and alteration halos. Exceptions include TiO_2, CaO, and SO_3. CaO and SO_3 abundances in the alteration are due to abundant crystalline calcium sulfates and amorphous sulfate phases, which likely were precipitated at least in part after the SiO_2 enrichment diagenetic event (Frydenvang et al., 2017; Yen et al., 2017). TiO_2 is generally immobile during diagenesis (e.g., Yen et al., 2017), and the reduced abundance of TiO_2 in the alteration halos could be due to passive reduction as other oxides such as SiO_2 are added to the halo. Similar geochemical trends were observed with ChemCam and APXS on an unnamed alteration halo (Figures 1b and 8d) in the Murray formation near Bridger Basin (Banham et al., 2018). These geochemical similarities are consistent with these materials being part of a shared diagenetic system during amorphous phase formation.

Using the Murray formation's 3° northwest regional dip (Kite et al., 2013; Lewis & Turner, 2019), we extrapolated the elevation of the Marias Pass high-SiO_2/low-FeO_T bedrock to the locations of the Stimson alteration halos Lubango (in Naukluft Plateau, Figure 8c) as well as Greenhorn and an unnamed alteration halo (in/near Bridger Basin, Figure 8d). We find that the high-SiO_2/low-FeO_T bedrock projects ~18 m below Lubango, ~2 m below Greenhorn, and ~1.5 m below the unnamed alteration halo. The close proximity

of these alteration halos to the underlying high-SiO_2/low-FeO_T bedrock supports the hypothesis that this bedrock layer is the source of SiO_2 enrichment for the alteration halos (Frydenvang et al., 2017). If the alteration halos are in fact genetically related to the high-SiO_2/low-FeO_T bedrock, this implies that the high-SiO_2/low-FeO_T bedrock layer extends throughout the area spanned by Marias Pass, Bridger Basin, and Naukluft Plateau (about 1 km, Figure 1b).

Alteration halos were also observed earlier in the traverse, ~53–55 m below and ~4.9 km northeast of Marias Pass in the Bradbury group. In this area, between sols 383 and 409, anomalously low Σ_{abs} were detected by several DAN active measurements, consistent with high-SiO_2/low-FeO_T material. These alteration halos lie ~11 m below the elevation to which the high-SiO_2/low-FeO_T bedrock projects from Marias Pass, given the regional dip of the Murray formation. The Bradbury group could either underlie the Murray formation or be coeval (deposited at the same time) with it (Grotzinger et al., 2015); so the relationship between these alteration halos and those in the Murray formation above Marias Pass is unknown. If the Bradbury group underlies the Murray formation stratigraphy, then the presence of these alteration halos at their observed location could indicate (1) a change in structural dip direction or magnitude between Marias Pass and these alteration halos, (2) the mobilization of SiO_2 downsection instead of upsection as with the Murray/Stimson alteration halos, or (3) the presence of a distinct high-SiO_2 reservoir underlying these Bradbury group alteration halos. If the Bradbury group is coeval with the Murray formation and represents a more proximal environment to the distal lacustrine Murray (Grotzinger et al., 2015), then the presence of these alteration halos below the projected elevation of Marias Pass suggests that they are related to a distinct, underlying high-SiO_2 reservoir.

4.1.3. Relationship to Orbital Detections of Hydrated SiO_2

Seelos et al. (2014) and Fraeman et al. (2016) used the orbital Compact Reconnaissance Imaging Spectrometer for Mars (CRISM) hyperspectral instrument to identify three locations (Sites β, γ, and δ in Figure 1a) near the MSL traverse which exhibit spectral signatures consistent with hydrated SiO_2. These detections are based on absorptions at 1.4 μm (OH), 1.9 μm (H_2O), and 2.2 μm (Si-OH), which are consistent with either hydrated SiO_2 glass or opal (Mustard et al., 2008; Rapin et al., 2018). Site β is ~8 km southwest of Marias Pass, Site γ is ~9.5 km northeast of Marias Pass, and Site δ is about 1 km south of Marias Pass (Figure 1a). Marias Pass and Sites β and γ are approximately colinear from southwest to northeast (azimuth 054). Since the Murray formation has a northwest regional dip (Kite et al., 2013; Lewis & Turner, 2019) that is nearly perpendicular to this line, these deposits may be bedrock exposures of the high-SiO_2/low-FeO_T layer discovered in Marias Pass. Marias Pass lies ~20 m above Site β and ~80 m above Site γ (Figure 8e). If these sites share a common stratigraphic layer with Marias Pass, the maximum regional dip of this layer along this azimuth is constrained to <0.5° to the southwest or northeast, in agreement with the regional northwest dip direction. A similar analysis shows that Site δ and Marias Pass would lie on the same stratigraphic horizon with a regional dip ~3.5° northwest, also in good agreement with the ~3° northwest regional dip. These orbital detections expand the observed extent of high-SiO_2 bedrock over an area at least 17.5 km wide, which strongly favors a stratigraphically conformable relationship within the Murray formation, and a depositional origin.

4.2. Hydration of High-SiO_2 Material

4.2.1. Comparison to Other Data Sets

ChemCam also can determine hydrogen abundances, though the LIBS spot size is significantly smaller than the DAN field of view. Hydrogen abundances measured by ChemCam are typically reported as H_2O, calculated in the same way as DAN WEH values. The mean hydration of 14 high-SiO_2 targets measured by ChemCam in the Lion area is 4.0 ± 1.2 wt.% H_2O. No DAN measurements were taken in this exact location, but the 1.85 ± 0.13 wt.% mean WEH measured by DAN in Marias Pass indicates that this ChemCam result is not representative of average Marias Pass high-SiO_2/low-FeO_T material. In contrast, DAN active measurements centered over the Lubango fracture alteration halo show a bulk halo hydration (~5.1 ± 1.0 wt.% WEH) that agrees well with ChemCam results from within the Lubango drill sample (4.0 ± 1.2 wt.% H_2O) (Rapin et al., 2018).

The much smaller field of view for individual ChemCam targets is potentially responsible for the discrepancy between DAN and ChemCam results in Marias Pass. The DAN field of view is a volume bounded by an ~1.5 m radius footprint on the surface and extends to a depth of ~50 cm. ChemCam, on the other hand, ablates material from points 350–550 μm in diameter to a depth of <600 μm (Wiens et al., 2012). Unfortunately, no DAN active measurement was taken in coincidence with ChemCam targets in the Lion area. But given

that the 14 high-SiO_2 ChemCam targets in the Lion area were within a 1.5 m radius, it is likely that the ChemCam results are representative of this area, comparable in size to a DAN field of view. Thus, while the bulk H_2O of the 3 m wide Lion area is well represented by ChemCam results, DAN WEH results represent a bulk view spanning Marias Pass over a few tens of meters.

The SAM tunable mass spectrometer aboard Curiosity also measures water content (sourced from both H_2O and OH^-) via EGA (Sutter et al., 2017). SAM measured 1.8 ± 0.9 wt.% H_2O from the Buckskin sample, which agrees well with our results. However, possible partial dehydration prior to SAM analysis (Rapin et al., 2018) could indicate that the Buckskin sample was significantly more hydrated prior to sample handling, consistent with the ChemCam H_2O results for high-SiO_2 Murray targets in the Lion area. SAM EGA data can also be used to understand the hydrated phases present in a sample. The Buckskin sample shows three evolved water temperature peaks. The first, at <400 °C, is likely due to H_2O evolved from opal-A; the second is from an unidentified source that could be jarosite (though in abundance below the CheMin detection limit); and the third, broadest peak, above ~500 °C is attributed to inclusion water in the amorphous fraction, which is likely to be a volcanic glass component based on CheMin XRD analysis (Sutter et al., 2017). As we demonstrate in the following section, significant contributions to evolved water from both opal-A and glass are consistent with our conclusion that both amorphous phases contain a significant fraction of the WEH measured by DAN. Sutter et al. (2017) also reports EGA results for H_2 and H_2S from the Buckskin sample, but these species (each <0.01 wt.%) do not make significant contributions to the WEH measured by DAN.

4.2.2. Constraints on Amorphous SiO_2 Phase Abundances

Due to a lack of hydrous crystalline phases in the Buckskin drill sample, the water content of the high-SiO_2 Murray material is contained in the amorphous phase (Rapin et al., 2018). The Buckskin drill sample contained 60 wt.% amorphous material, which had a SiO_2 abundance of 77 wt.%, based on CheMin and APXS mineralogical and geochemical analyses (Morris et al., 2016). The broad XRD amorphous peak in Buckskin is consistent with a mixture of ~6 wt.% opal-CT and ~33 wt.% opal-A and/or rhyolitic glass in the bulk sample (Morris et al., 2016; Rampe et al., 2017), which accounts for the large SiO_2 abundance of the amorphous fraction. Based on the presence of opal-CT, Morris et al. (2016) argue that the volcanic glass has been altered wholly or in part to opal-A.

The irregular structure of amorphous SiO_2 phases provides sites for H_2O and OH^- to bind and fill voids, which are lacking in microcrystalline (e.g., chalcedony) and macrocrystalline (quartz) phases (Smith et al., 2013). Most terrestrial opals contain 4–9 wt.% water (Segnit et al., 1965), whereas SiO_2 glasses on Earth only hold up to 3 wt.% H_2O (Graetsch et al., 1994; Newman et al., 1986; Rapin et al., 2018). Rapin et al. (2018) describes a correlation between hydrogen and SiO_2 abundances in the high-SiO_2 Murray material at Marias Pass. Using a ChemCam-derived hydration of 4.0 ± 1.3 wt.% H_2O for Buckskin, they predict that the measured hydrogen resides in opal-A and conclude that the Buckskin opal-A has a maximum hydration of 8.0 ± 2.6 wt.% H_2O. But our significantly lower DAN-derived WEH value suggests there may be a significant volcanic glass component in Marias Pass.

Using the mean bulk hydration measured by DAN (1.85 ± 0.13 wt.% WEH) and other geochemical and mineralogical constraints, we can calculate a minimum abundance of SiO_2 glass in the high-SiO_2/low-FeO_T material at Marias Pass. In a system of n hydrated phases, we calculate the abundance of the ith hydrated phase by solving

$$\sum_{i=1}^{n} [\mathrm{WEH}]_i[i] = [\mathrm{WEH}]_{bulk}$$

where $[\mathrm{WEH}]_i \equiv$ wt. fraction WEH of the ith phase and $[\mathrm{i}] \equiv$ bulk abundance of the ith phase. To obtain the minimum abundance of SiO_2 glass we assume a maximum hydration of 3 wt.% WEH in the glass (Graetsch et al., 1994; Newman et al., 1986; Rapin et al., 2018), a ferrihydrite hydration of 4.0 wt.% WEH (Gabriel et al., 2018), and an opal hydration of 7.4 ± 1.6 wt.% H_2O reported by Rapin et al. (2018) for the opal-A in high-SiO_2 fracture alteration halos that was shown to be consistent with targeted DAN experiments of those features. Rapin et al. (2018) has shown that hydrogen abundance is correlated with SiO_2 abundance in ChemCam high-SiO_2 Murray targets, indicating that only minor water is contained in non-SiO_2 phases. For this reason, we do not include non-SiO_2 hydrous phases except ferrihydrite reported by Morris et al. (2016). Ferrihydrite abundance in the Buckskin drill sample is limited to ~1.7 wt.% (by available FeO_T in the amorphous fraction) and accounts for a maximum of 0.07 wt.% WEH. Given these constraints and assumptions, we find

the minimum abundance of SiO_2 glass in the high-SiO_2/low-FeO_T material to be 15.0 ± 13.5 wt.%. The possible presence of other hydrated amorphous phases, such as amorphous sulfates, would reduce the water inventory available for the SiO_2 phases and shift the glass-to-opal ratio toward more abundant glass, thus supporting our conclusion that 15.0 ± 13.5 wt.% SiO_2 glass is a minimum abundance. The present retention of at least minor SiO_2 glass supports the silicic volcaniclastic origin of this material.

4.3. Origin of SiO_2-rich Sediments and Implications for Mars Magmatic History

The presence of silicic glass and opal along with tridymite in a discrete stratigraphic interval in Marias Pass strongly suggests that this material is derived from an evolved igneous protolith. Hydrated SiO_2 has been identified in many locations on Mars in addition to Gale crater (e.g., Glotch et al., 2006; Milliken et al., 2008; Mustard et al., 2008; Squyres et al., 2008; Sun & Milliken, 2015; Weitz et al., 2011). Multiple pathways for SiO_2 enrichment in Martian environments have been proposed, including active enrichment through SiO_2 sintering (Frydenvang et al., 2017; Ruff et al., 2011; Skok et al., 2010), passive enrichment through acid leaching (McAdam et al., 2008; Squyres et al., 2008; Weitz et al., 2011; Yen et al., 2017), and fractional crystallization in an evolved magmatic system (Carter & Poulet, 2013; Christensen et al., 2005; Edwards et al., 2017; McCubbin et al., 2008; Udry et al., 2014, 2018). The crystalline mineralogy of the Buckskin sample is consistent with a silicic volcanic deposit from an evolved source (Morris et al., 2016; Rampe et al., 2017). Alternatively, it has been proposed that tridymite and cristobalite could form in nonvolcanic environments on Earth, but no such mineral deposits have been unambiguously documented. For instance, tridymite and cristobalite were inferred in a terrestrial deep-sea chert by Klasik (1975). This identification was based on a visual resemblance in photomicrographs; however, XRD experiments were unable to detect these minerals, possibly due to low abundances.

Without plate tectonics, other mechanisms must be invoked to produce evolved magma on Mars. One possible mechanism is mantle plumes that "shut off." Hawaiian volcanism provides a terrestrial analog for this mechanism. The Hawaiian-Emperor seamount chain consists of volcanic edifices fed by a mantle plume beneath the overriding Pacific plate. When a volcanic edifice is transported away from its mantle plume source, the magma supply decreases and shallow magma reservoirs solidify. Deeper magma reservoirs persist but are cut off from the plume source and can produce more evolved magmas through crystal fractionation of the deep magma chambers (Clague & Sherrod, 2014). On Mars, a mantle plume cannot be cut off from an associated volcanic edifice due to plate motion, but mantle plumes do "shut off," possibly resulting in evolved magmas as at terrestrial hot spots that are cut off from their mantle plumes.

But experiments and simulations have shown that it is not necessary to "shut off" a mantle plume to produce evolved magma on Mars. Experiments conducted by McCubbin et al. (2008) demonstrated that a wet basaltic magma (1.67 wt.% water) at the base of a thick Martian crust can be enriched in SiO_2 up to an intermediate igneous composition through a single stage of fractional crystallization. Additionally, experiments have shown that intraplate magmatism can differentiate a tholeiitic basaltic parent melt to a rhyolitic composition (Whitaker et al., 2007), and ChemCam analyses of float rocks and conglomerate clasts in Gale crater (Cousin et al., 2017) follow compositional trends consistent with this magmatic evolution (Edwards et al., 2017). Further, simulations conducted by Udry et al. (2018) demonstrated that these Gale crater felsic compositions are consistent with mantle melting and fractional crystallization in intraplate magmatism.

In the presence of water, opaline SiO_2 is expected to alter to quartz under typical Martian surface conditions in <400 Ma (Tosca & Knoll, 2009) following the typical SiO_2 diagenesis pathway: glass → opal-A → opal-CT → chalcedony → quartz (e.g., Smith et al., 2013; Tosca & Knoll, 2009; Williams et al., 1985). Opaline SiO_2 deposits observed on Mars today have likely experienced only intermittent, if any, contact with liquid water since their formation (Tosca & Knoll, 2009). The presence of opal-CT in the Buckskin drill sample and minor (~1 wt.%) quartz in the Lubango fracture alteration halo indicate that diagenetic alteration of opal-A did occur in these materials, but the present retention of opal-A in both the bedrock and alteration halos indicates that diagenesis did not proceed to completion and that these materials have been in contact with liquid water for <400 Ma since the formation of secondary amorphous phases (McLennan et al., 2019; Tosca & Knoll, 2009).

Opaline SiO_2 in the Buckskin drill sample could be either detrital (Morris et al., 2016) or a product of tridymite/cristobalite alteration (Hurowitz et al., 2017). Due to the large fraction of detrital igneous sediment and the likelihood that the amorphous component of high-SiO_2 material is a mixture of volcanic glass and its alteration products, Hurowitz et al. (2017) suggests that mudstone sediments in Gale crater are sourced

from igneous provinces and are not recycled sediments. This suggests that the high-SiO_2 material in Marias Pass is the product of erosion from a primary SiO_2-rich volcanic source rock in the Gale lake catchment. The fine laminations observed in Marias Pass high-SiO_2 material are consistent with density sorting of sediment in a lacustrine environment, which would carry less dense, SiO_2-rich clasts to more distal sections of the lake (Hurowitz et al., 2017). Edwards et al. (2017) suggested that larger float rocks observed earlier in the MSL traverse were sourced from regions closer to Gale crater than the generally finer-grained mafic mudstones, but the observation of a high-SiO_2/low-FeO_T mudstone layer suggests that more distal felsic sources could also have contributed.

A weak correlation exists between ChemCam-derived SiO_2 abundance and chemical index of alteration (CIA) in the Murray formation (Bedford et al., 2019). CIA is a measure of how chemically altered a sample is. Due to the postdepositional alteration of the high-SiO_2 Murray in Marias Pass (see section 1.3), Bedford et al. (2019) did not include these data in their CIA analyses. This correlation is not significant enough to explain the variations in SiO_2 observed within the Murray formation, suggesting that SiO_2 abundance in the Murray is likely a result of source region geochemistry. Based on larger CIA values, higher-SiO_2 abundances, and the presence of cristobalite (in the Telegraph Peak and Buckskin drill samples) and tridymite (in the Buckskin drill sample), Bedford et al. (2019) argue that the Murray formation records a detrital contribution from a more evolved magmatic source that is not present in the Bradbury group. As Bedford et al. (2019) discusses, the higher Murray CIA values could be a result of the felsic mineralogy produced by an evolved magmatic source.

The SiO_2 abundance in Marias Pass is significantly larger than in the Murray stratigraphy above or below it, suggesting a temporal evolution of source region during Murray deposition. The low density of tridymite and cristobalite allows these minerals to remain entrained in fluviolacustrine systems longer than basaltic sediments. Therefore, the source of these minerals could be relatively distant from the Murray formation (Bedford et al., 2019). The nitrate and oxychlorine contents of the Buckskin sample are greater than other Murray samples analyzed by SAM EGA, also suggesting an alternate (or additional) source for this material (Sutter et al., 2017), possibly due to an evolving fluvial catchment feeding Gale lake.

The tridymite and SiO_2-rich glass in Marias Pass could also have been deposited as sediment derived from impact melt. However, the high abundance of tridymite and SiO_2 in Marias Pass would require a significant sedimentary fractionation by relative density if the tridymite-bearing impact melt formed in typical Martian basaltic crust. Alternatively, the impact melt could have been enriched in SiO_2 at the time of formation, but this would likely require an impact into a region of preexisting high-SiO_2 material, requiring another SiO_2 enrichment mechanism preceding the impact, though compositional segregation of impact melt is also possible (Bouska & Bell III, 1993). Terrestrial and lunar impact melts are typically enriched in Al and depleted in Si (Bouska & Bell III, 1993), inconsistent with the SiO_2-rich, Al_2O_3-poor material in Marias Pass.

Palucis et al. (2014) mapped a >1000 km^2 catchment outside of Gale crater that fed Peace Vallis, an 80 km^2 alluvial fan between the Curiosity traverse and the Gale crater rim to the northwest. Like the Murray formation, the Peace Vallis fan was deposited in the Late Noachian/Early Hesperian (Palucis et al., 2014). If the drainage network that fed Peace Vallis was active during the deposition of the Murray formation, it would have provided an evolving sediment source as the network incised into the plains north of Gale crater. This catchment area may have included ash fall deposits related to volcanic plains further north (Palucis et al., 2014), and this is a possible source of the tridymite-bearing material in Marias Pass. An extensive fluvial network entering Gale crater from the south is another possible sediment source.

The lateral extent, thickness, and conformable expression of the high-SiO_2/low-FeO_T layer mapped throughout Marias Pass, in addition to its genetic relationship to fracture alteration halos up to 1 km away and the orbital detection of likely coeval outcrops over a several kilometer range, all support the hypothesis, originally based on the detection of tridymite in the Buckskin drill sample (Morris et al., 2016), that this material is volcanic in origin and therefore the product of an evolved magma source, rather than being the result of passive or active SiO_2 enrichment during diagenetic alteration like the high-SiO_2 alteration halos upsection. The stratigraphic correlation of Marias Pass with outcrops nearly 10 km away to both the southwest and northeast, as well as an outcrop 1 km to the south, which is consistent with the regional dip of the Murray

formation, provides remarkable evidence for a laterally extensive, stratigraphically bound interval of silicic volcaniclastic sediments within the Murray formation.

5. Conclusions

Using ChemCam and APXS geochemistry to create subsurface models for DAN simulations, we have identified and mapped a thick layer of high-SiO_2/low-FeO_T material in the Murray formation throughout Marias Pass. Mastcam multispectral analysis of a large outcrop, predicted to be high-SiO_2/low-FeO_T material based on our DAN results, is consistent with a high-SiO_2/low-FeO_T composition and shares spectral characteristics with known high-SiO_2/low-FeO_T material like that exposed in the Lion area. A single subhorizontal layer can project through all high-SiO_2/low-FeO_T material observed in Marias Pass, and the thickness of this layer is at least 1 m. A probable genetic link between the high-SiO_2/low-FeO_T bedrock in Marias Pass and high-SiO_2 fracture alteration halos is suggested by geochemical similarities and geometric relationships. This genetic link indicates that the high-SiO_2/low-FeO_T bedrock extends throughout the region spanned by Marias Pass and these alteration halos, or about 1 km. Orbital detections from CRISM of hydrated SiO_2 material 1–10 km to the south, southwest, and northeast of Marias Pass are approximately stratigraphically equivalent to Marias Pass assuming an ~3° regional dip to the northwest. These outcrops are likely additional exposures of the high-SiO_2/low-FeO_T bedrock investigated in Marias Pass indicating that the high-SiO_2/low-FeO_T material exposed in Marias Pass is laterally extensive over at least a 17.5 km distance.

The DAN-derived WEH for the high-SiO_2/low-FeO_T material is significantly lower than that from ChemCam data in Marias Pass. This is likely due to heterogeneities in opal abundance throughout Marias Pass. The DAN result of 1.85 ± 0.13 wt.% WEH represents the bulk hydration over tens of meters. This hydration suggests that a lower-hydration phase is present in addition to opal-A. SAM EGA temperature release profiles suggest that both rhyolitic glass and opal were present in the Buckskin drill sample. Assuming a maximum SiO_2 glass WEH content of 3 wt.%, we calculate that there is a minimum SiO_2 glass abundance of 15.0 ± 13.5 wt.%.

The Buckskin drill sample from the stratigraphic layer described here contains tridymite. This, along with our determinations of the large areal extent and thickness of this layer, its stratigraphically conformable expression, and its inferred volcanic glass component, indicates that it is a volcaniclastic product derived from felsic igneous rock. Though felsic compositions have been observed in several regions on Mars, it is not well understood how evolved magmas could form. Mechanisms to shut off Martian mantle plumes are not well understood, but would provide a mechanism for the production of evolved magmas on Mars, as seen in intraplate volcanism on Earth. A few other mechanisms have also been suggested that could produce these evolved compositions on Mars. This study is the first example of *in situ* mapping of a silicic volcaniclastic layer and description of its compositional and stratigraphic characteristics on another planet. Similar future applications of this neutron spectroscopy technique on landed missions can help resolve questions that still persist regarding the production of evolved magmatic bodies on Mars.

Acknowledgments
The authors are grateful to JPL for developing and operating the MSL Curiosity rover mission and to the Mars Science Laboratory team for facilitating the multinational collaboration involving scientists from the United States, Denmark, France, Russia, and Canada to synthesize results from several MSL instrument data sets to make this work possible. We also would like to individually thank Marion Nachon, Abigail Fraeman, and Vivian Sun for helpful conversations regarding aspects of this work. This work was supported by the Mars Science Laboratory Participating Scientist Program, the Los Alamos National Laboratory Center for the Study of Earth and Space, the NASA Earth and Space Exploration Fellowship, the Elwha Stipend of Western Washington University, and the Carlsberg Foundation. The authors acknowledge Research Computing at Arizona State University for providing HPC, storage, etc., resources that have contributed to the research results reported within this paper (URL: http://www.researchcomputing.asu.edu). All data used for this work are available on the NASA Planetary Data System via links on the MSL page (URL: https://pds-geosciences.wustl.edu/missions/msl/).

References

Abercrombie, S. P., Menzies, A., Abarca, H. E., Luo, V. X., Samochina, S., Trautman, M. T., et al. (2019). Multi-platform immersive visualization of planetary, asteroid, and terrestrial analog terrain. *Lunar and Planetary Science L*, *2268*.

Agee, C. B., Wilson, N. V., McCubbin, F. M., Ziegler, K., Polyak, V. J., Sharp, Z. D., et al. (2013). Unique meteorite from early Amazonian Mars: Water-rich basaltic breccia Northwest Africa 7034. *Science*, *339*, 780–785. https://doi.org/10.1126/science.1228858

Bandfield, J. L., Hamilton, V. E., & Christensen, P. R. (2000). A global view of Martian surface compositions from MGS-TES. *Science*, *287*(5458), 1626–1630. https://doi.org/10.1126/science.287.5458.1626

Banham, S. G., Gupta, S., Rubin, D. M., Watkins, J. A., Sumner, D. Y., Edgett, K. S., et al. (2018). Ancient Martian aeolian processes and palaeomorphology reconstructed from the Stimson formation on the lower slope of Aeolis Mons, Gale crater, Mars. *Sedimentology*, *65*(4), 993–1042. https://doi.org/10.1111/sed.12469

Bedford, C. C., Bridges, J. C., Schwenzer, S. P., Wiens, R. C., Rampe, E. B., Frydenvang, J., & Gasda, P. J. (2019). Alteration trends and geochemical source region characteristics preserved in the fluviolacustrine sedimentary record of Gale crater, Mars. *Geochimica et Cosmochimica Acta*, *246*, 234–266. https://doi.org/10.1016/j.gca.2018.11.031

Bell III, J. F., Godber, A., McNair, S., Caplinger, M. A., Maki, J. N., Lemmon, M. T., et al. (2017). The Mars Science Laboratory Curiosity rover Mastcam instruments: Preflight and in-flight calibration, validation, and data archiving. *Earth and Space Science*, *4*(7), 396–452. https://doi.org/10.1002/2016EA000219

Bouska, V., & Bell III, J. F. (1993). Assumptions about the presence of natural glasses on Mars. *Journal of Geophysical Research*, *98*(E10), 18,719–18,725. https://doi.org/10.1029/93JE01959

Calef III, F., & Parker, T. (2016). MSL Gale merged orthophoto mosaic. PDS Annex, U.S. Geological Survey.

Campbell, J. L., King, P. L., Burkemper, L., Berger, J. A., Gellert, R., Boyd, N. I., et al. (2014). The Mars Science Laboratory APXS calibration target: Comparison of Martian measurements with the terrestrial calibration. *Nuclear Instruments and Methods in Physics Research B*, *323*, 49–58. https://doi.org/10.1016/j.nimb.2014.01.011

Carter, J., & Poulet, F. (2013). Ancient plutonic processes on Mars inferred from the detection of possible anorthositic terrains. *Nature Geoscience*, *6*, 1008–1012. https://doi.org/10.1038/NGEO1995

Christensen, P. R., McSween Jr., H. Y., Bandfield, J. L., Ruff, S. W., Rogers, A. D., Hamilton, V. E., et al. (2005). Evidence for magmatic evolution and diversity on Mars from infrared observations. *Nature*, *436*, 504–509. https://doi.org/10.1038/nature03639

Clague, D. A., & Sherrod, D. R. (2014). Growth and degradation of Hawaiian volcanoes. *U.S. Geological Survey Professional Paper*, *1801*, 97–146.

Clark, R. N., King, T. V. V., Klejwa, M., & Swayze, G. A. (1990). High spectral resolution reflectance spectroscopy of minerals. *Journal of Geophysical Research*, *95*(B8), 12,653–12,680. https://doi.org/10.1029/JB095iB08p12653

Clegg, S. M., Wiens, R. C., Anderson, R., Forni, O., Frydenvang, J., Lasue, J., et al. (2017). Recalibration of the Mars Science Laboratory ChemCam instrument with an expanded geochemical database. *Spectrochimica Acta Part B: Atomic Spectroscopy*, *129*, 64–85. https://doi.org/10.1016/j.sab.2016.12.003

Cousin, A., Sautter, V., Payré, V., Forni, O., Mangold, N., Gasnault, O., et al. (2017). Classification of igneous rocks analyzed by ChemCam at Gale crater, Mars. *Icarus*, *288*, 265–283. https://doi.org/10.1016/j.icarus.2017.01.014

Edwards, P. H., Bridges, J. C., Wiens, R., Anderson, R., Dyar, D., Fisk, M., et al. (2017). Basalt-trachybasalt samples in Gale Crater, Mars. *Meteoritics & Planetary Science*, *52*(11), 2391–2410. https://doi.org/10.1111/maps.12953

Fedo, C., Grotzinger, J., Gupta, S., Stein, N. T., Watkins, J., Banham, S., et al. (2017). Facies Analysis and Basin Architecture of the Upper Part of the Murray Formation, Gale Crater, Mars. *Lunar and Planetary Science XLVIII*, *1689*.

Foreman-Mackey, D., Hogg, D. W., Lang, D., & Goodman, J. (2013). Emcee: The MCMC Hammer. *Publications of the Astonomical Society of the Pacific*, *125*(925), 306–312. https://doi.org/10.1086/670067

Fraeman, A. A., Ehlmann, B. L., Arvidson, R. E., Edwards, C. S., Grotzinger, J. P., & Milliken, R. E. (2016). The stratigraphy and evolution of lower Mount Sharp from spectral, morphological, and thermophysical orbital data sets. *Journal of Geophysical Research: Planets*, *121*, 1713–1736. https://doi.org/10.1002/2016JE005095

Frydenvang, J., Gasda, P. J., Hurowitz, J. A., Grotzinger, J. P., Wiens, R. C., Newsom, H. E., et al. (2017). Diagenetic silica enrichment and late-stage groundwater activity in Gale crater, Mars. *Geophysical Research Letters*, *44*, 4716–4724. https://doi.org/10.1002/2017GL073323

Gabriel, T. S. J, Hardgrove, C., Czarnecki, S., Rampe, E. B., Rapin, W., Achilles, C. N., et al. (2018). Water abundance of dunes in Gale Crater, Mars from active neutron experiments & implications for amorphous phases. *Geophysical Research Letters*, *45*, 12,766–12,775. https://doi.org/10.1029/2018GL079045

Gasda, P. J., DeLapp, D. M., Mcinroy, R. E., Wiens, R. C., Bridges, J. C., Edwards, P. H., et al. (2016). Identification of fresh feldspars in Gale Crater using ChemCam. *Lunar and Planetary Science XLVII*, *1604*.

Glotch, T. D., Bandfield, J. L., Christensen, P. R., Calvin, W. M., McLennan, S. M., Clark, B. C., et al. (2006). Mineralogy of the light-toned outcrop at Meridiani Planum as seen by the Miniature Thermal Emission Spectrometer and implications for its formation. *Journal of Geophysical Research*, *111*, E12S03. https://doi.org/10.1029/2005JE002672

Graetsch, H., Gies, H., & Topalović, I. (1994). NMR, XRD and IR study on microcrystalline opals. *Physics and Chemistry of Minerals*, *21*, 166–175. https://doi.org/10.1007/BF00203147

Gross, J., & Filiberto, J. (2014). Granitic compositions in gabbroic Martian meteorite NWA 6963: Evidence for extreme fractional crystallization of a hydrous magma. *Workshop on Volatiles in the Martian Interior*, *1015*.

Grotzinger, J. P., Gupta, S., Malin, M. C., Rubin, D. M., Schieber, J., Siebach, K., et al. (2015). Deposition, exhumation, and paleoclimate of an ancient lake deposit, Gale crater, Mars. *Science*, *350*(6257), aac7575. https://doi.org/10.1126/science.aac7575

Grotzinger, J. P., Sumner, D. Y., Kah, L. C., Stack, K., Gupta, S., Edgar, L., Rubin, D., et al. (2014). A habitable fluvio-lacustrine environment at Yellowknife Bay, Gale Crater, Mars. *Science*, *343*(6169), 1242777. https://doi.org/10.1126/science.1242777

Hardgrove, C., Moersch, J., & Drake, D. (2011). Effects of geochemical composition on neutron die-away measurements: Implications for Mars Science Laboratory's Dynamic Albedo of Neutrons experiment. *Nuclear Instruments and Methods in Physics Research A*, *659*(1), 442–455. https://doi.org/10.1016/j.nima.2011.08.058

Humayun, M., Nemchin, A., Zanda, B., Hewins, R. H., Grange, M., Kennedy, A., et al. (2013). Origin and age of the earliest Martian crust from meteorite NWA 7533. *Nature*, *503*, 513–516. https://doi.org/10.1038/nature12764

Hurowitz, J. A., Grotzinger, J. P., Fischer, W. W., McLennan, S. M., Milliken, R. E., Stein, N., et al. (2017). Redox stratification of an ancient lake in Gale crater, Mars. *Science*, *356*(6341), eaah6849. https://doi.org/10.1126/science.aah6849

Jun, I., Mitrofanov, I., Litvak, M. L., Sanin, A. B., Kim, W., Behar, A., et al. (2013). Neutron background environment measured by the Mars Science Laboratory's Dynamic Albedo of Neutrons instrument during the first 100 sols. *Journal of Geophysical Research: Planets*, *118*, 2400–2412. https://doi.org/10.1002/2013JE004510

Kite, E. S., Lewis, K. W., Lamb, M. P., Newman, C. E., & Richardson, M. I. (2013). Growth and form of the mound in Gale Crater, Mars: Slope wind enhanced erosion and transport. *Geology*, *41*(5), 543–546. https://doi.org/10.1130/G33909.1

Klasik, J. A. (1975). High cristobalite and high tridymite in a middle Eocene deep-sea chert. *Science*, *189*(4203), 631–632. https://doi.org/10.1126/science.189.4203.631

Le Deit, L., Hauber, E., Fueten, F., Pondrelli, M., Rossi, A. P., & Jaumann, R. (2013). Sequence of infilling events in Gale Crater, Mars: Results from morphology, stratigraphy, and mineralogy. *Journal of Geophysical Research: Planets*, *118*, 2439–2473. https://doi.org/10.1002/2012JE004322

Lewis, K. W., & Turner, M. L. (2019). Geologic structure of the Vera Rubin Ridge, Gale Crater, Mars. *Lunar and Planetary Science L*, *2216*.

Litvak, M. L., Mitrofanov, I. G., Barmakov, Yu. N., Behar, A., Bitulev, A., Bobrovnitsky, Yu., et al. (2008). The Dynamic Albedo of Neutrons (DAN) experiment for NASA's 2009 Mars Science Laboratory. *Astrobiology*, *8*(3), 605–612. https://doi.org/10.1089/ast.2007.0157

Malin, M. C., Ravine, M. A., Caplinger, M. A., Ghaemi, F. T., Schaffner, J. A., Maki, J. N., et al. (2017). The Mars Science Laboratory (MSL) Mast cameras and Descent imager: Investigation and instrument descriptions. *Earth and Space Science*, *4*(8), 506–539. https://doi.org/10.1002/2016EA000252

Mangold, N., Thompson, L. M., Forni, O., Williams, A. J., Fabre, C., Le Deit, L., et al. (2016). Composition of conglomerates analyzed by the Curiosity rover: Implications for Gale Crater crust and sediment sources. *Journal of Geophysical Research: Planets*, *121*, 353–387. https://doi.org/10.1002/2015JE004977

Maurice, S., Wiens, R. C., Saccoccio, M., Barraclough, B., Gasnault, O., Forni, O., et al. (2012). The ChemCam instrument suite on the Mars Science Laboratory (MSL) Rover: Science objectives and mast unit description. *Space Science Reviews*, *170*, 95–166. https://doi.org/10.1007/s11214-012-9912-2

McAdam, A. C., Zolotov, M. Y., Mironenko, M. V., & Sharp, T. G. (2008). Formation of silica by low-temperature acid alteration of Martian rocks: Physical-chemical constraints. *Journal of Geophysical Research*, *113*, E08003. https://doi.org/10.1029/2007JE003056

McCubbin, F. M., Nekvasil, H., Harrington, A. D., Elardo, S. M., & Lindsley, D. H. (2008). Compositional diversity and stratification of the Martian crust: Inferences from crystallization experiments on the picrobasalt Humphrey from Gusev Crater, Mars. *Journal of Geophysical Research*, *113*, E11013. https://doi.org/10.1029/2008JE003165

McLennan, S. M., Grotzinger, J. P., Hurowitz, J. A., & Tosca, N. J. (2019). The sedimentary cycle on early Mars. *Annual Review of Earth and Planetary Sciences*, *47*, 91–118. https://doi.org/10.1146/annurev-earth-053018-060332

McSween Jr., H. Y. (1984). SNC meteorites: Are they Martian rocks? *Geology*, *12*(1), 3–6. https://doi.org/10.1130/0091-7613(1984)12<3:SMATMR>2.0.CO;2

McSween Jr., H. Y. (2015). Petrology on Mars. *American Mineralogist*, *100*(11–12), 2380–2395. https://doi.org/10.2138/am-2015-5257

McSween, H. Y., Wyatt, M. B., Gellert, R., Bell III, J. F., Morris, R. V., Herkenhoff, K. E., et al. (2006). Characterization and petrologic interpretation of olivine-rich basalts at Gusev Crater, Mars. *Journal of Geophysical Research*, *111*, E02S10. https://doi.org/10.1029/2005JE002477

Milliken, R. E., Swayze, G. A., Arvidson, R. E., Bishop, J. L., Clark, R. N., Ehlmann, B. L., et al. (2008). Opaline silica in young deposits on Mars. *Geology*, *36*(11), 847–850. https://doi.org/10.1130/G24967A.1

Mitrofanov, I. G., Litvak, M. L., Varenikov, A. B., Barmakov, Y. N., Behar, A., Bobrovnitsky, Y. I., et al. (2012). Dynamic Albedo of Neutrons (DAN) experiment onboard NASA's Mars Science Laboratory. *Space Science Reviews*, *170*, 559–582. https://doi.org/10.1007/s11214-012-9924-y

Morris, R. V., Vaniman, D. T., Blake, D. F., Gellert, R., Chipera, S. J., Rampe, E. B., et al. (2016). Silicic volcanism on Mars evidenced by tridymite in high-SiO_2 sedimentary rock at Gale crater. *Proceedings of the National Academy of Sciences of the United States of America*, *113*(26), 7071–7076. https://doi.org/10.1073/pnas.1607098113

Mustard, J. F., Murchie, S. L., Pelkey, S. M., Ehlmann, B. L., Milliken, R. E., Grant, J. A., et al. (2008). Hydrated silicate minerals on Mars observed by the Mars Reconnaissance Orbiter CRISM instrument. *Nature*, *454*, 305–309. https://doi.org/10.1038/nature07097

Mustard, J. F., Poulet, F., Gendrin, A., Bibring, J.-P., Langevin, Y., Gondet, B., et al. (2005). Olivine and pyroxene diversity in the crust of Mars. *Science*, *307*(5715), 1594–1597. https://doi.org/10.1126/science.1109098

Nachon, M., Mangold, N., Forni, O., Kah, L. C., Cousin, A., Wiens, R. C., et al. (2017). Chemistry of diagenetic features analyzed by ChemCam at Pahrump Hills, Gale crater, Mars. *Icarus*, *281*, 121–136. https://doi.org/10.1016/j.icarus.2016.08.026

Newman, S., Stolper, E. M., & Epstein, S. (1986). Measurement of water in rhyolitic glasses: Calibration of an infrared spectroscopic technique. *American Mineralogist*, *71*(11-12), 1527–1541.

Palucis, M. C., Dietrich, W. E., Hayes, A. G., Williams, R. M. E., Gupta, S., Mangold, N., et al. (2014). The origin and evolution of the Peace Vallis fan system that drains to the Curiosity landing area, Gale Crater, Mars. *Journal of Geophysical Research: Planets*, *119*, 705–728. https://doi.org/10.1002/2013JE004583

Rampe, E. B., Ming, D. W., Blake, D. F., Bristow, T. F., Chipera, S. J., Grotzinger, J. P., et al. (2017). Mineraology of an ancient lacustrine mudstone succession from the Murray formation, Gale crater, Mars. *Earth and Planetary Science Letters*, *471*, 172–185. https://doi.org/10.1016/j.epsl.2017.04.021

Rapin, W., Chauviré, B., Gabriel, T. S. J., McAdam, A. C., Ehlmann, B. L., Hardgrove, C., et al. (2018). In situ analysis of opal in Gale crater, Mars. *Journal of Geophysical Research: Planets*, *123*, 1955–1972. https://doi.org/10.1029/2017JE005483

Rice, M. S., Bell III, J. F., Cloutis, E. A., Wang, A., Ruff, S. W., Craig, M. A., et al. (2010). Silica-rich deposits and hydrated minerals at Gusev Crater, Mars: Vis-NIR spectral characterization and regional mapping. *Icarus*, *205*(2), 375–395. https://doi.org/10.1016/j.icarus.2009.03.035

Ruff, S. W., Farmer, J. D., Calvin, W. M., Herkenhoff, K. E., Johnson, J. R., Morris, R. V., et al. (2011). Characteristics, distribution, origin, and significance of opaline silica observed by the Spirit rover in Gusev crater, Mars. *Journal of Geophysical Research*, *116*, E00F23. https://doi.org/10.1029/2010JE003767

Sears, V. F. (1992). Neutron scattering lengths and cross sections. *Neutron News*, *3*(3), 26–37. https://doi.org/10.1080/10448639208218770

Seelos, K. D., Seelos, F. P., Viviano-Beck, C. E., Murchie, S. L., Arvidson, R. E., Ehlmann, B. L., & Fraeman, A. A. (2014). Mineralogy of the MSL Curiosity landing site in Gale crater as observed by MRO/CRISM. *Geophysical Research Letters*, *41*, 4880–4887. https://doi.org/10.1002/2014GL060310

Segnit, E. R., Stevens, T. J., & Jones, J. B. (1965). The role of water in opal. *Journal of the Geological Society of Australia*, *12*(2), 211–226. https://doi.org/10.1080/00167616508728593

Singer, R. B., McCord, T. B., Clark, R. N., Adams, J. B., & Huguenin, R. L. (1979). Mars surface composition from reflectance spectroscopy: A summary. *Journal of Geophysical Research*, *84*(B14), 8415–8426. https://doi.org/10.1029/JB084iB14p08415

Skok, J. R., Mustard, J. F., Ehlmann, B. L., Milliken, R. E., & Murchie, S. L. (2010). Silica deposits in the Nili Patera caldera on the Syrtis Major volcanic complex on Mars. *Nature Geoscience*, *3*, 838–841. https://doi.org/10.1038/NGEO990

Smith, M. R., Bandfield, J. L., Cloutis, E. A., & Rice, M. S. (2013). Hydrated silica on Mars: Combined analysis with near-infrared and thermal-infrared spectroscopy. *Icarus*, *223*(2), 633–648. https://doi.org/10.1016/j.icarus.2013.01.024

Squyres, S. W., Arvidson, R. E., Ruff, S., Gellert, R., Morris, R. V., Ming, D. W., et al. (2008). Detection of silica-rich deposits on Mars. *Science*, *320*(5879), 1063–1067. https://doi.org/10.1126/science.1155429

Stack, K. M., Grotzinger, J. P., Lamb, M. P., Gupta, S., Rubin, D. M., Kah, L. C., et al. (2019). Evidence for plunging river plume deposits in the Pahrump Hills member of the Murray formation, Gale crater, Mars. *Sedimentology*, *66*(5), 1768–1802. https://doi.org/10.1111/sed.12558

Sun, V. Z., & Milliken, R. E. (2015). Ancient and recent clay formation on Mars as revealed from a global survey of hydrous minerals in crater central peaks. *Journal of Geophysical Research: Planets*, *120*, 2293–2332. https://doi.org/10.1002/2015JE004918

Sutter, B., McAdam, A. C., Mahaffy, P. R., Ming, D. W., Edgett, K. S., Rampe, E. B., et al. (2017). Evolved gas analyses of sedimentary rocks and eolian sediment in Gale Crater, Mars: Results of the Curiosity rover's sample analysis at Mars instrument from Yellowknife Bay to the Namib Dune. *Journal of Geophysical Research: Planets*, *122*, 2574–2609. https://doi.org/10.1002/2016JE005225

Taylor, G. J., Martel, L. M. V., Karunatillake, S., Gasnault, O., & Boynton, W. V. (2010). Mapping Mars geochemically. *Geology*, *38*(2), 183–186. https://doi.org/10.1130/G30470.1

Thomson, B. J., Bridges, N. T., Milliken, R., Baldridge, A., Hook, S. J., Crowley, J. K., et al. (2011). Constraints on the origin and evolution of the layered mound in Gale Crater, Mars using Mars Reconnaissance Orbiter data. *Icarus*, *214*, 413–432. https://doi.org/10.1016/j.icarus.2011.05.002

Tosca, N. J., & Knoll, A. H. (2009). Juvenile chemical sediments and the long term persistence of water at the surface of Mars. *Earth and Planetary Science Letters*, *286*(3-4), 379–386. https://doi.org/10.1016/j.epsl.2009.07.004

Udry, A., Balta, J. B., & McSween Jr., H. Y. (2014). Exploring fractionation models for Martian magmas. *Journal of Geophysical Research: Planets*, *119*, 1–18. https://doi.org/10.1002/2013JE004445

Udry, A., Gazel, E., & McSween Jr., H. Y. (2018). Formation of evolved rocks at Gale crater by crystal fractionation and implications for Mars crustal composition. *Journal of Geophysical Research: Planets*, *123*, 1525–1540. https://doi.org/10.1029/2018JE005602

Vaniman, D. T., Martínez, G. M., Rampe, E. B., Bristow, T. F., Blake, D. F., Yen, A. S., et al. (2018). Gypsum, bassanite, and anhydrite at Gale crater, Mars. *American Mineralogist*, *103*(7), 1011–1020. https://doi.org/10.2138/am-2018-6346

Weitz, C. M., Bishop, J. L., Thollot, P., Mangold, N., & Roach, L. H. (2011). Diverse mineralogies in two troughs of Noctis Labyrinthus, Mars. *Geology*, *39*(10), 899–902. https://doi.org/10.1130/G32045.1

Werner, C. J., Armstrong, J., Brown, F. B., Bull, J. S., Casswell, L., Cox, L. J., et al. (2018). MCNP user's manual: Code version 6.2. LA-UR-17-29981.

Whitaker, M. L., Nekvasil, H., Lindsley, D. H., & Difrancesco, N. J. (2007). The role of pressure in producing compositional diversity in intraplate basaltic magmas. *Journal of Petrology*, *48*(2), 365–393. https://doi.org/10.1093/petrology/egl063

Wiens, R. C., Maurice, S., Barraclough, B., Saccoccio, M., Barkley, W. C., Bell III, J. F., et al. (2012). The ChemCam instrument suite on the Mars science laboratory (MSL) rover: Body unit and combined system tests. *Space Science Reviews*, *170*, 167–227. https://doi.org/10.1007/s11214-012-9902-4

Williams, L. A., Parks, G. A., & Crerar, D. A. (1985). Silica diagenesis, I. Solubility controls. *Journal of Sedimentary Petrology*, *55*(3), 301–311. https://doi.org/10.1306/212F86AC-2B24-11D7-8648000102C1865D

Wray, J. J., Hansen, S. T., Dufek, J., Swayze, G. A., Murchie, S. L., & Seelos, F. P. (2013). Prolonged magmatic activity on Mars inferred from the detection of felsic rocks. *Nature Geoscience*, *6*, 1013–1017. https://doi.org/10.1038/NGEO1994

Wyatt, M. B., & McSween Jr., H. Y. (2002). Spectral evidence for weathered basalt as an alternative to andesite in the northern lowlands of Mars. *Nature*, *417*, 263–266. https://doi.org/10.1038/417263a

Yen, A. S., Ming, D. W., Vaniman, D. T., Gellert, R., Blake, D. F., Morris, R. V., et al. (2017). Multiple stages of aqueous alteration along fractures in mudstone and sandstone strata in Gale Crater, Mars. *Earth and Planetary Science Letters*, *471*, 186–198. https://doi.org/10.1016/j.epsl.2017.04.033